A STUDY OF RADIATION-INDUCED PULMONARY FIBROSIS (RIPF) IN MOUSE MODELS USING DIAGNOSTIC IMAGING

by

Daniel R. McIlrath

A Thesis

Submitted to the Faculty of Purdue University

In Partial Fulfillment of the Requirements for the degree of

Doctor of Philosophy

School of Health Sciences

West Lafayette, Indiana

May 2020

THE PURDUE UNIVERSITY GRADUATE SCHOOL
STATEMENT OF COMMITTEE APPROVAL

Dr. Carlos Perez-Torres, Chair

Department of Health and Human Sciences

Dr. Ulrike Dydak

Department of Health and Human Sciences

Dr. Craig Goergen

Weldon School of Biomedical Engineering

Dr. Jonathan Shannahan

Department of Health and Human Sciences

Approved by:

Dr. Aaron Bowman

Dedicated to my wife, Miriam. Thank you for your love and encouragement.

TABLE OF CONTENTS

LIST OF TABLES

LIST OF FIGURES

ABSTRACT

Radiation-induced lung injury (RILI) is a common condition in the setting of lung and breast cancer. Often, patients who suffer from RILI experience pneumonitis and pulmonary fibrosis months after treatment. These pathologies have commonly been modeled using mice and observing their deterioration until mortality and quantifying pathology on histological sections.

With this study, we used a longitudinal microCT and a 7T MRI to characterize male C57Bl/6 mice irradiated with a single dose of 20 Gy to the whole thoracic area delivered by an X-Rad cabinent irradiator. CT was performed with a respiratory gating sequence at 2 week timepoints to construct an RIPF model. The fraction of RIPF to total lung volume was calculated at each time point from images, and the data was anaylzed using one-way ANOVA Welch and Dunnett's T3 multiple comparisons tests. Tidal lung volumes were also calculated and anlyazed in a simlar manner. Mice were then imaged using MRI and CT at 0, 5, and 8 week timepoints to compare results. These results were analyzed for comparison (ANOVA and Dunnett's T3) and correlation (Pearson's r) with each other. Histology was later performed using H&E and Trichrome stains to provide ex-vivo verification of pathology. At the 10-12 week time point ($p = 0.05, \alpha = 0.05$) significant RIPF formed. Weeks proceeding showed increased significance until the 22+ week timepoint, which showed less statistical significance ($p = 0.353$) due to increased variance at this timepoint. Dunnett's T3 test showed no significant differences between tidal lung volumes over time. Tests also showed no significant differences between CT and MRI results with a correlation coefficient of $r = 0.343$. Early in the study, problems arose when pre-marture mortality was occurring to a significant portion of our subjects. Analysis later showed issues during irradiation that resulted in significant dose being absorbed by the stomach. Adjusting our shiedling lead to increased early survival of our subjects enabling us to contine our study. Significant RIPF development was not significant until 10-12 weeks post-irradiation, then RIPF became more severe at proceeding timepoints. Tidal lung volume showed no significant deviation over the development of RIPF. This result is most likely affected by the variation of results at later timepoints, since several mice with severe RIPF were significantly hindered in their ability to breathe during the study. MRI results showed close correlation with CT results and prodcued similar values at early timepoints. However, noticeable differences were seen at later timepoints when significant RIPF developed ($CT = 0.4618, MRI = 0.2338$).

CHAPTER 1: INTRODUCTION

Radiation Induced Lung Injury

Lung and breast cancer are the two most diagnosed cancers each year, numbering almost 3 million cases in recent years.[1–3] As a means of treatment, over 50% of patients with thoracic malignancies are prescribed a regimen of radiation therapy to combat the cancerous tumors.[4,5] Despite the effectiveness of the treatment, issues can arise post-therapy when significant radiation dose is incurred by more than the targeted tumor. Healthy lung tissue is at risk of being injured during treatments, so oncology teams work to minimize doses to the healthy tissue as much as possible while maximizing doses to the tumor. However, despite best efforts, the lung tissue can still absorb large enough doses to become injured. In as many as 35% of cases, radiation-induced lung injury can occur.[6–10] The two primary sequela are pulmonary pneumonitis and pulmonary fibrosis. Considered the more acute pathology, radiation-induced pulmonary pneumonitis (RIPP) occurs 1-3 months post-treatment and can last as long as 6 months.[5] Radiation-induced pulmonary fibrosis (RIPF) is considered the more chronic pathology, typically presenting as early as 6 months post-treatment and developing for up to two years. [4,5,11] RIPF is the more concerning injury of the two pathologies due to its permanence once contracted and its high average incidence rate reported to be between 16-18%.[4,7,11]

Symptoms

As previously stated, over 50% of patients diagnosed with a thoracic cancer are prescribed some regimen of radiation therapy. Consequential to this therapy, radiation-induced lung injuries may present post-treatment with the two phases: an acute phase of RIPP after 1 month and a chronic phase of RIPF after 6 months. The presentation and diagnoses of these phases are somewhat similar; however, there are key attributes to differentiate and characterize the phases.

In the acute phase, most patients do not present with any symptoms. RIPP can be minimal and resolve without with any need for intervention. In the cases where patients are symptomatic, they may present with dyspnea, coughing, a low-grade fever, or chest

discomfort.[5,12,13] Typical treatment for RIPP is corticosteroids to reduce inflammation and relieve symptoms.

In the late phase, RIPF occurs resulting from the pro-inflammatory and pro-fibrotic mechanisms. Some studies cite RIPF as a result of RIPP and unresolved inflammation,[5,12,14] however, more recent studies show no dependence between the two.[7,15] Also, patients are mostly asymptomatic early in the phase, possibly presenting with progressive dyspnea, dry cough, *cor pulmonale*, or pulmonary hypertension.[5,13]

Due to the asymptomatic nature of the phases, it is important for patients to have routine check-ups with diagnostic imaging at the discretion of the physician to assure no injuries are developing.

Factors Effecting RIPF

Three primary factors can affect the occurrence and severity of RIPF: treatment, tumor location, and patient characteristics. Treatment delivery is the primary factor in RIPF pathogenesis. Beginning at 20 Gy, RIPF should be considered as a possible sequalae. Fractionation greatly aids in minimizing risk, but RIPF is still a risk with higher doses per fraction. Furthermore, characterized as a parallel organ, the lungs are very sensitive to volume effects. Treatment fields that encase greater volumes of the lung as opposed to small areas of higher dose will greatly increase the risk of RIPF.[25] The location of the tumor can also impact RIPF pathogenesis if it is near more sensitive structures such as the mediastinum, proximal bronchi, heart, esophagus, or nerves. [5,13] The patient's history also factors in to his/her risk of developing RIPF. Pre-existing lung conditions or possible genetic susceptibility may increase the patient's risk of contracting RIPF.[5,13,26]

Imaging RIPF

In order to observe the lung and its structures *in vivo*, CT has long been the standard for lung imaging due to its great signal-to-noise ratio (SNR) of air with tissue and superior spatial resolution.[4,8,16,17] MRI typically struggles to produce images of structures within the lung because it consists primarily of air.

Lung CT

CT imaging utilizes ionizing radiation to formulate an image through differing objects' linear attenuation coefficients (μ). By delivering radiation through an object, the radiation will pass through various tissues and anatomy of differing valued μ determined by the structure's density. A detector is used to collect the resulting attenuated radiation beam and information of an X-ray's attenuation through a certain path. CTs then collate this information over many paths through the same object by altering the angle of incidence the radiation beam is delivered. An image is then reconstructed by using the collected intensities detected and backprojecting them through the corresponding beam's path and forming an image (**Fig. 1**).

Image contrast for CT is primarily dependent on objects' densities compared to water's density. When adjacent structures have similar densities, CT images are unable to contrast the two structures. However, lung tissue has vastly different density from the surrounding air within the lungs – tissue such as the bronchioles have densities close to water while the air is much less dense. This is the primary reason CT is the standard for imaging the lungs and RIPF.

The unit used for CT intensities is Hounsfield units defined as:

$$HU = 1000 \times \frac{\mu - \mu_{water}}{\mu_{water} - \mu_{air}}$$

H^1 Anatomical Lung MRI

Although MRI is considered the frontier for diagnostic imaging, it is rarely used for lung imaging. This is primarily due to the intrinsic characteristic of air molecules in magnetic fields.[18,19]

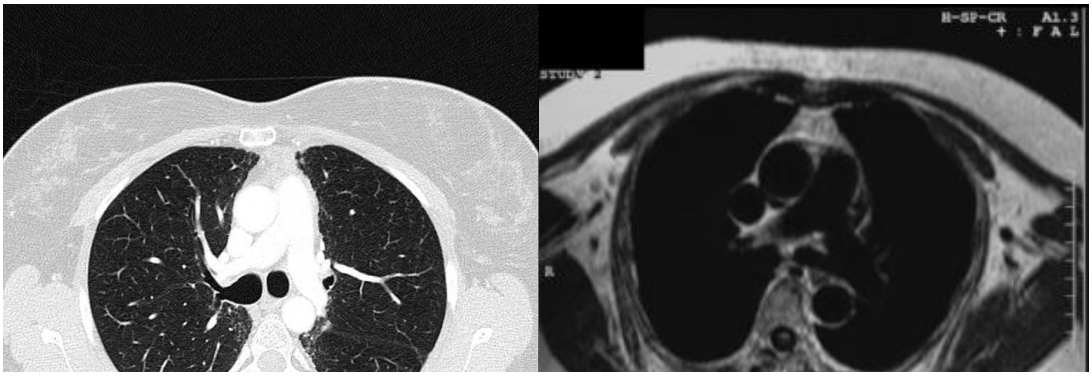

Figure 1: **[L]** Axial CT image of a human lung. The bronchi and bronchioles are noticeable features within the lung due to CT's great spatial resolution and tissue-air contrast. **[R]** Axial MR image of a human lung using a typical pulse sequence. No signal is produced from within the lung due to air's short transverse relaxation time (T2). *Case courtesy of Dr Mohammad Taghi Niknejad, Radiopaedia.org, rID: 61444*

Air has an extremely short transverse magnetization relaxation time which decays so quickly, most scan sequences are unable to acquire any discernable signal.[19] Since the lungs are primarily filled with air, MR images of the lungs show extreme hypointensity since minimal signal is detected (**Fig. 2**). In order to obtain signal from the lungs with an MRI, a scan sequence needs to shorten its time-to-echo (TE) value to fractions of a millisecond ($< 0.5\ ms$)[19] – this sequence is known as the ultra-short TE sequence (UTE). The advent of this imaging sequence has allowed for MR images of structures with generally short T2 times such as ligaments and tendons.[19] With a UTE sequence, acquirable signals of structures within the lung are generated and captured for image reconstruction. However, a major limitation of MRI of the lungs is the sensitivity to motion which requires the scan to be performed within a single breath-hold. Patients with severe lung disease may not be able to hold their breath long enough for the acquisition of quality MRI datasets.

Alternate Lung MRI Techniques

In addition to traditional proton-based MR imaging, alternative imaging techniques exist to image the lungs by using hyperpolarized gasses, typically Helium-3 and Xeon-129, where their nuclear spins are artificially aligned despite typically low spin-densities.[20] The advantage to utilizing these isotopes to image the lungs is their ability to provide a higher particle density than protons in the lung and offer comparatively slower decay times. Utilizing these gases generates functional imaging that enables non-invasive functional lung analyses such as ventilation dynamics, perfusion, and alveolar-capillary diffusion (**Fig. 2**).[20,21]

Flourine-19 is a similar isotope that can be utilized for non-invasive functional imaging; however, ^{19}F does not have to be hyperpolarized due to its similar gyromagnetic ratio to protons, γ~40.05 MHz/T and γ~42.58 MHz/T respectively. Utilization of these isotopes is a means to map anatomical, functional, and metabolic changes associated with lung injuries and further develop pre-clinical injury models.[22,23] In the case of RIPF, decreased ventilation should occur in areas that are fibrotic due to the loss of elasticity. Utilizing one of these isotopes overlaid with an anatomical ^{1}H image would allow for functional validation of RIPF with corresponding anatomical presentation.

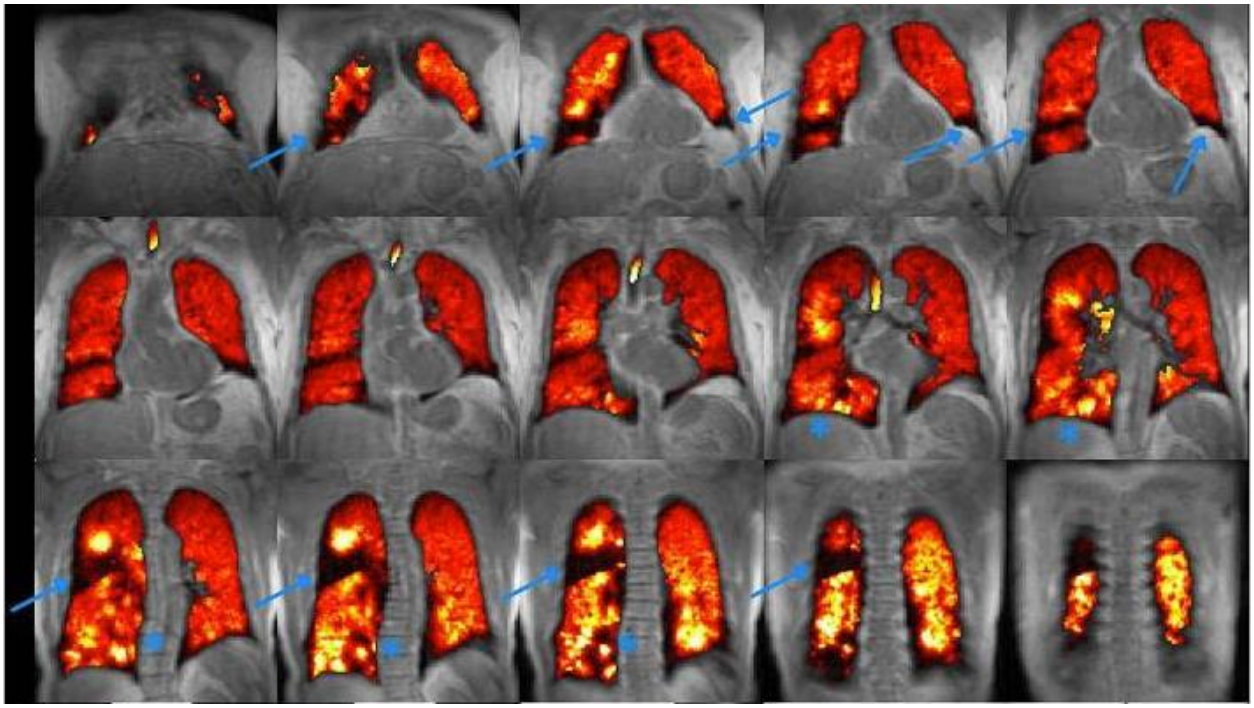

Figure 2: COPD patient's hyperpolarized ^{129}Xe ventilation images with ^{1}H anatomical images overlaid. Blue areas point to areas of ventilation defects.[20]

Image Characteristics of Radiation-Induced Lung Disease

Early phase presentation of RIPP appears as homogeneous, glassy hyperdense areas on CT images (**Fig. 3c-d**). These areas are typically confined to the treatment volume and do not conform to anatomical boundaries.[5,24] Further development of these areas appears as discrete consolidation growth which is indicative of the late, RIPF phase (**Fig. 3e-f**).

Late phase presentation of RIPF appears as consolidation of sharp, delineated areas of hyperdensity. Within these areas, air bronchograms – air-filled bronchi presenting against hyperdense regions – and bronchiectasis are typical features (**Fig. 3g-h**).[14] Progression of RIPF has been observed for up to 24 months post-treatment but typically plateaus at this time. Structural shifts and volume loss are expected and, consequently, patients present with severe dyspnea. RIPF is irreversible; therefore, treatment is only palliative. Steroids can be used to reduce swelling which may lesson symptoms and respiration rehabilitation is performed to aid

the patient in more effective breathing techniques. In more serious cases, a lung transplant may be necessary.

MRI's presentation of RIPP and RIPF is less known due to CT's dominance in diagnosis the pathology. However, given air's extremely short transverse relaxation times and pathology typically presents with more fluid- or tissue- like characteristics, MR images will generate pathology-air contrast if abundant enough and signal collection occurs early in the pulse sequence. RIPP would most likely be difficult to image using conventional ^{1}H MRI due its scarcity, but RIPF would be consolidated and hyperdense enough to generate a signal and appear hyperintense on an ultra-short TE scan. Physical characteristics should present similar as in CT images – sharp, delineated areas of hyperintensity.

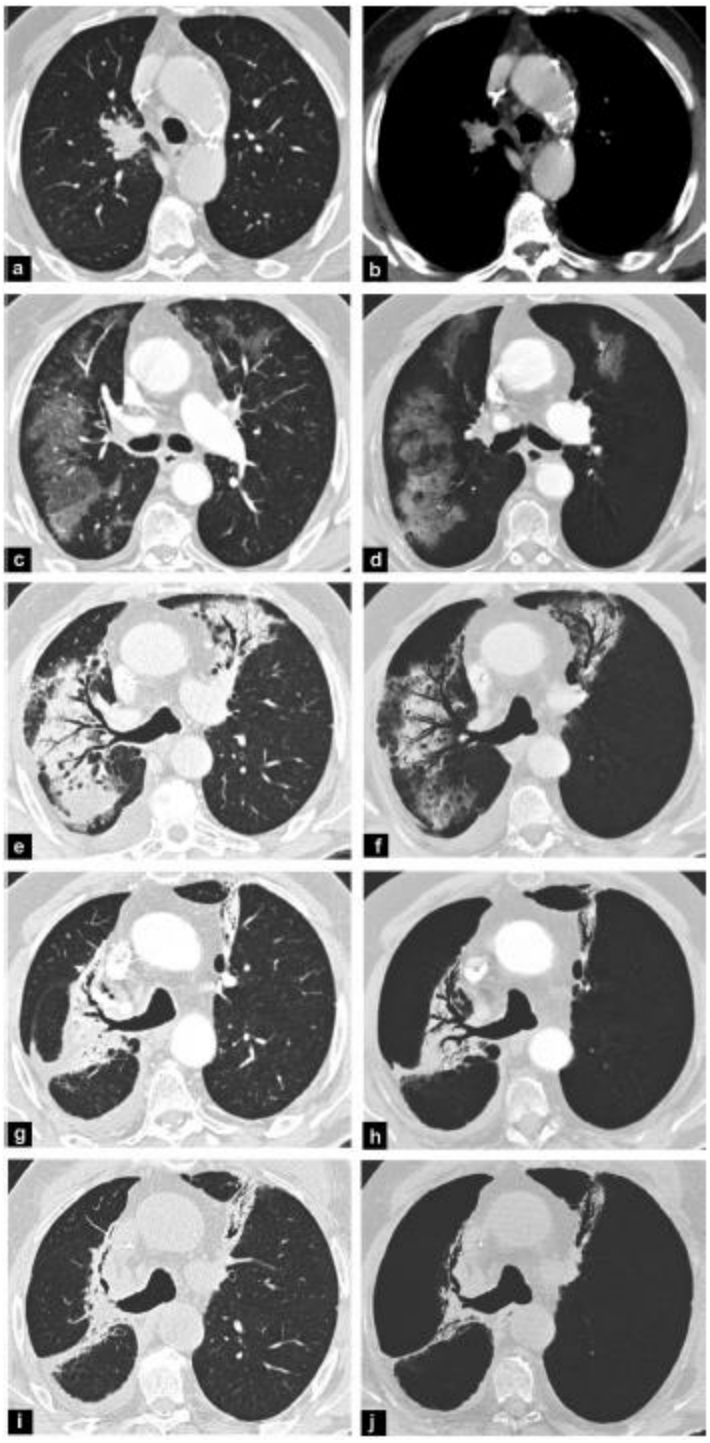

Figure 3: (**a-b**) Radiation-induced lung disease (RILD) after 2D-RT for lung cancer in the upper right lobe. (**c-d**) Homogeneous, glassy hyperdense areas present as RIPP. (**e-f**) Consolidation of these areas occurs indicating RIPF development. (**g-j**) RIPF presents with air bronchograms and bronchiectasis as well as more discrete borders. [5]

Human vs. Mouse Lung Anatomy

Although several earlier studies may have overlooked RIPF's influence in patients' health, more recent studies have acknowledged the need to model RIPF using murine models.[11,27–29] Murine models allow for researchers to better understand disease pathogenesis and presentation which provides researchers a tool for pre-clinical treatment studies. These studies, in turn, benefit clinicians by leading to new or more effective treatments that revolutionize patient care and prognosis. To better understand these models, and the need for them, it is important to have a sufficient background of lung anatomy and the current understanding of RIPF pathogenesis.

In order to evaluate murine lung models, it is important to have a brief overview of lung anatomy and its appearance in Computed Tomography (CT) and Magnetic Resonance Imaging (MRI). A sufficient understanding of the lung's gross anatomy and appearance in diagnostic images will aid in reading the subsequent chapters.

Lungs consist of several lobes that make up the left and right lung (**Fig 1**). Human and mouse lungs have several similarities in their structure; however, there are some significant differences – most notably is the number of lobes that make up both sides of the lung. Humans have 3 lobes on the right (superior, middle, inferior lobes) and 2 lobes on the left (superior, inferior lobes), while mice have 4 lobes on the right (cranial, middle, caudal, accessory lobes) and 1 lobe on the left (left lobe).

Similarly to humans, mice have a trachea that terminates caudal to the heart and bifurcates into the left and right primary extrapulmonary bronchi before entering the lung parenchyma. For humans, upon entering the lung parenchyma, the intrapulmonary bronchi branch out into the bronchioles to supply the different lobes of the lung. However, in mice, the extrapulmonary bronchi form into bronchioles upon entrance into the lung parenchyma – differentiated from the bronchi by their absence of cartilage. These bronchioles branch off in an asynchronous and monopodial pattern compared to human's dichotomous branching pattern. These bronchioles

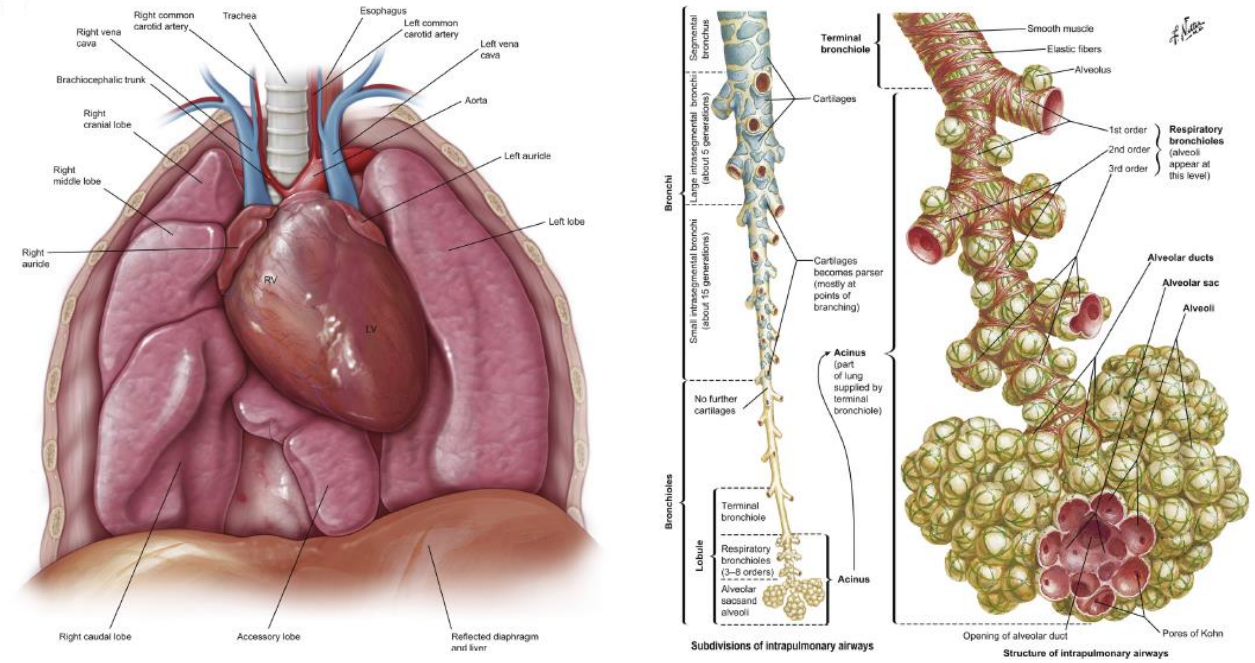

Figure 4: **[L]** Gross anatomy of a mouse's lung. Dissimilar to human lungs, the right side consists of 4 lobes (cranial, middle, caudal, and accessory) and the left side consists of a single lobe. **[R]** The bronchi and bronchioles of a mouse – the air pathways guiding oxygen to the alveoli. At the end of the bronchioles are the alveoli where gas exchange occurs to oxygenate blood in nearby capillaries. [15]

terminate into the alveolar sacs and alveoli. It is here, deemed the respiratory zone, that gas exchange occurs between the alveoli and capillaries to oxygenate the blood.[30]

Latent Period and RIPF Pathogenesis

To further understand RIPF and its models, it is important to know the molecular mechanisms that lead to its pathogenesis from a healthy lung. Although these mechanisms are not fully understood, many studies have researched possible molecular proponents of RIPF in hope of illuminating its occurrence. These studies have focused namely on inflammatory cytokines that

are also associated with RIPP.[7,15,29] These cytokines are detected and believed to influence fibrosis development at the cellular level, so it is important to elucidate the cellular framework of the lungs and the cells functionalities.

The smallest structure of the lung's gross anatomy is the alveoli – the tiny air sacs of the lung where gas exchange occurs delivering oxygen to and carbon dioxide away from the blood. [30] The alveoli consist of a simple epithelial layer surrounded by an extracellular matrix, a surfactant layer to minimize friction between the air and tissue, macrophages for immune response, pneumocytes to produce surfactant and promote gas exchange, and fibroblasts for cell growth and

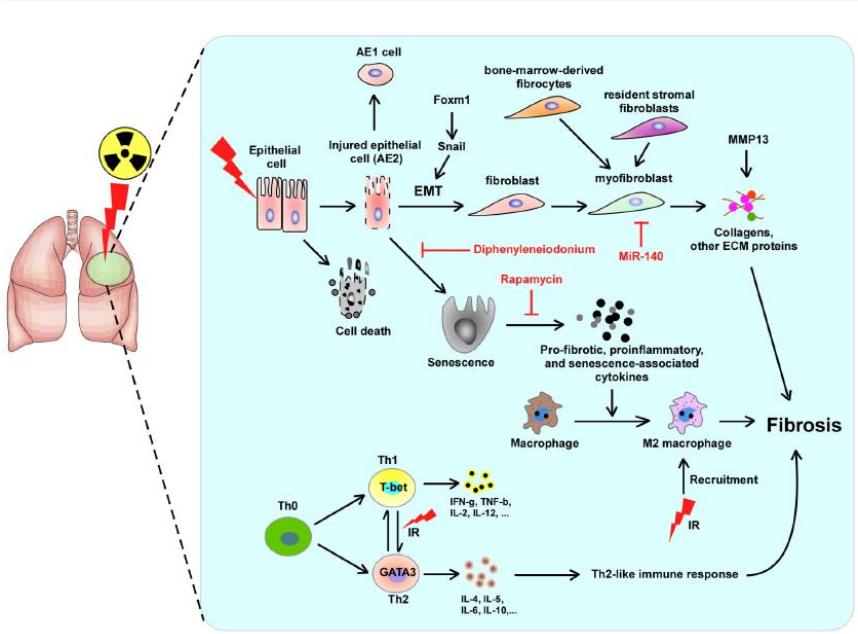

Figure 5: Three primary pathways exist in the pathogenesis of RIPF. Primarily, pro-immune and pro-inflammatory responses occur after radiation injury to epithelial cells leads to M2 macrophage influx or myofibroblast differentiation. Alternatively, radiation can cause immune response cells (Th0) to be differentiated into Th1 and Th2 cells that secrete pro-fibrotic cytokines. [7]

repair.[9,30]

When lung tissue absorbs ionizing radiation, cell DNA becomes damaged and disrupts functionality while also destroying structures.[31] Three pro-fibrotic pathways can be modeled with the known molecular mechanisms (**Fig. 3**).[7] Two pathways branch from the radiation damage occurring to the lung's epithelial cells. From this damage, cell senescence can occur that produces pro-fibrotic and pro-inflammatory cytokines differentiating lung macrophages into M2 macrophages that accumulate in the lung. In addition to M2 macrophage influx, damaged epithelial cells promote myofibroblast differentiation which develops collagen for tissue repair and, if over-

regulated, fibrosis. Independent of the epithelial cell damage, an immune response from CD4+ T-helper (Th0) cells leads to the secretion of several pro-fibrotic and pro-inflammatory cytokines that exacerbate RIPF pathogenesis.[7,15]

To summarize, large doses of ionizing radiation lead to dysregulation of the alveoli cell's functionalities that over time develops into the observed RIPP and RIPF. This dysregulation is not an abrupt occurrence and takes time to manifest into any pathology, thus appearing as a latent period despite the activity occurring at the molecular level. For RIPF to develop, fibroblasts and myofibroblasts (transformed fibroblasts) accumulate in the lung and develop access amounts of collagen in an attempt to restore structure to the injured extracellular matrix. These excess collagen deposits form into fibrosis that inhibits lung functionality and prevents gas exchange between the lungs and capillaries. Transformation of fibroblasts into myofibroblasts can best be explained by "pro-fibrotic stimuli" that signal the transformation and promote excess repair.[9,10] This process occurs over several months that eventually leads to observable scaring on the lungs.

Previous Murine Studies

The majority of radiation murine studies have utilized whole thoracic irradiations (WTI) with the C57Bl/6 mouse strain.[11] WTIs have shown the greatest popularity among studies (roughly 83%),[11] most likely due to their simplicity and being able to irradiate the entire volume of the lung while avoiding dose to any other structures. Other studies have performed partial lung irradiations as well as whole body irradiations. The frequent use of C57Bl/6 mice in RIPF studies has been attributable to more historical reasons than anything else. Previous studies have frequently used this strain of mice believed to be "pro-fibrotic."[11] With so many studies utilizing this strain for RIPF research, it has perpetuated C57Bl/6 usage to allow comparison with previous studies.

As previously stated, majority of studies modeling RIPF in mice do so having used mortality as the end point – median survival time (MST) as their response variable. Numerous studies have observed MST's response to dose and modeled their relationship using both male and female C57Bl/6 mice.[11,32–36] Studies have ranged dose with a minimum of 15 Gy, reporting no RIPF development and fewer deaths at lower doses, up to 25 Gy. What is observed has been a negative relationship between MST and dose, and female mice have shown a greater radiosensitivity than male mice (**Fig. 5**).[11]

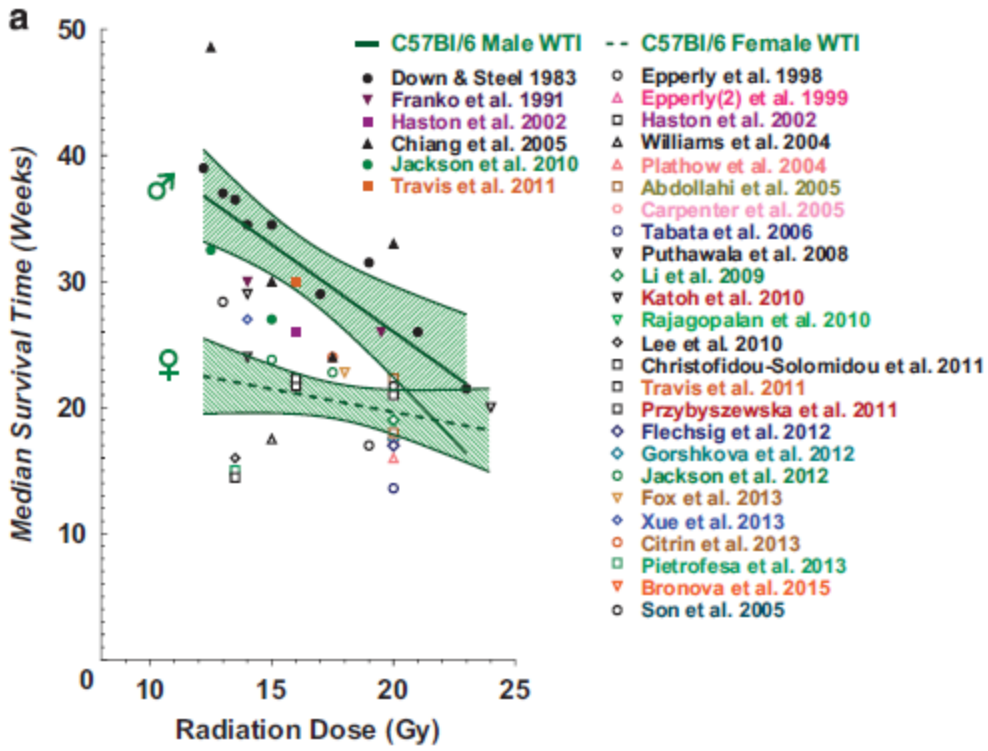

Figure 6: Aggregation of several radiation-induced lung disease studies tracking median survival time (MST) versus dose using male and female C57Bl/6 mice. [11]

An example of an early study was conducted in 1983 by Julian D. Down and G. Gordon Steel.[32] In this study they compared two mouse strains – C57Bl and CBA mice – response to varying amounts of dose delivered to the thorax with 230 kV X-rays. Their means to characterize response was primarily through MST with no additional qualifications. Even in more recent studies, the survival explanatory variable has dictated findings above any other variable. In Isabel L. Jackson's studies,[35,37] she developed models using percent survival to evaluate and compare results of different models being used to bridge animal models with the human lung for acute radiation exposures. While meaningful, models need to be characterized beyond the resulting end points to further detail and evaluate the pathology the lead to moratality. Intermediate characteristics of disease progression are clinically relevant and necessary to form a more well-rounded model.

Rationale and Aims

Despite all that is known about RIPF through years of studies and observations, little is understood of its detailed pathogenesis and no means of treatment exists for patients who develop it. The development of these models gains even more importance when applied to situations beyond the clinic. With nuclear disasters such as Chernobyl and Fukushima occurring within recent years and fears of nuclear warfare happening in the future, radiation injury studies are on the rise.[38]

Previous models have succeeded in characterizing the mortality rates and risks of RIPF associated with certain delivered doses. However, the research has led studies to focus beyond mortality, and focus instead on the latent period and understanding the molecular mechanisms that lead to RIPF. The belief here is that a knowledge of these pathways may expose a means of prevention if the correct mechanisms are inhibited. Several treatments such as selenium have been proposed to inhibit these pro-fibrotic pathways. [39] A base model is necessary for such treatments to prove effective, but these models are tedious to develop. With current models only characterizing RIPF using mortality endpoints, treatment studies are unable to analyze treatments intermediate effectiveness and determine time to onset. To do this, a quantifiable model needs to be developed to enable temporal analysis of treatments pre-mortality.

Without this quantifiable diagnostic RIPF model, these studies fail to be clinically relevant in their analysis and characterization of the pathology – clinics do not wait for patients' deaths in order to diagnose RIPF, they utilize imaging modalities to diagnose and track any lung injuries a patient may have. *In vivo* analysis needs to be performed in order mimic the clinic's methodolgy and provide a quantifiable temporal model. The best way to do this is by using CT.

CT is considered the "gold standard" by clinics for diagnosing post-RT sequalae. By using CT, we can image mice lungs post-irradiation to evaluate pathology over time. Since RIPF presents as consolidated hyperintense volumes, we can segment these areas and record their volumes. By tracking this volume over time, a timeline can be generated to characterize RIPF by the volume of consolidation in proportion to total lung volume.

Given a successfully developed RIPF CT model, time to onset of RIPF can be calculated to determine regions where drug intervention is plausible and provide a base model to test any drug intervention's effectiveness. Given RIPF irreversibility, it is important to determine time of onset to know when permanent damage begins to develop so preventative measures can be taken

before-hand. Our model will also provide average volumes of RIPF across time, so any experimental treatments can be tested by comparing their resulting average RIPF volumes against our standard model.

Although CT provides great spatial resolution to segment RIPF, consolidated hyperdense areas can be the result of more than RIPF. CT provides poor tissue characterization and is unable to distinguish between RIPF and tumor recurrence or infections.[5,40] Also, subjects have to incur more radiation with each CT scan that would add more harmful ionizing radiation dose. MR imaging provides better tissue characterization and dose-sparing, that would aid in forming a more sensitive model of RIPF. However, as previously stated, MRI does not image lung structures well without utilizing a UTE pulse sequence. We study whether this pulse sequence enables us to detect and quantify a signal so that a timeline of RIPF can be modeled.

In our study, we recognize RIPF develops to be radiologically noticeable around 10-12 post-irradiation with only 30% (n=10) developing significantly severe RIPF at 22 weeks. These subjects have discrepancies in how the severity of RIPF presented. This has led to a branching of two groups – rapid RIPF onset and chronic RIPF onset. Additionally, we are able to show MRI, when using a UTE scan sequence, can reproduce statistically reasonable results to the CT data with one exception – the one mouse subject that presents with rapid onset RIPF is not detected in our MR images. Lastly, we show our resolve of early issues in our study of pre-mature mortality in our subjects that prevented the continuation of our study. Upon closer inspection to our irradiation setup, it was noticed that subjects were not consistently placed relative to shielding and that the apertures in our shielding were too large relative to our subjects' thoraxes. This was only determined after subjects presented with distended stomachs on early CT image acquisitions. Altered aperture dimensions to contour closer to subjects' thoraxes led to a near 100% survival rate and the ability for our study to continue.

CHAPTER 2: QUANTIFICATION OF MURINE RADIATION-INDUCED PULMONARY FIBROSIS (RIPF) FROM WHOLE THORACIC IRRADATION

Daniel R. McIlrath, MS[1], Gianna Porro[1], Elizabeth Roach[1], and Carlos J. Perez-Torres, PhD[1,2*].
[1]*School of Health Sciences, Purdue University, West Lafayette, Indiana, US*
[2]*Purdue University Center for Cancer Research, Purdue University, West Lafayette, Indiana, US*

[1]Address for correspondence: School of Health Sciences, Purdue University, 550 Stadium Mall Drive, Hampton Hall 1263A, West Lafayette, IN 47907, USA; cperezto@purdue.edu

Abstract

Background: Mouse models of radiation-induced lung fibrosis (RIPF) are commonly produced to find novel treatments for the condition. However, current models fail to adequately replicate clinical methods in the analysis of RIPF by only tracking mortality rates. Clinics diagnose and track RIPF through CT scanning rather than observing time-to-death. Pre-clinical studies need to be more clinically relevant to ease experimental treatments' transitions into clinical trials.

Methods: Male C57Bl/6 mice (n=43) were irradiated with a single dose of 20 Gy to the whole thoracic area delivered by an 320 kV X-Rad cabient irradiator. CT was performed with respitory gating at 2 week timepoints and developd images to identify RIPF pathology *in vivo*. Confirmation of CT findings was performed via histology on the lungs using Mason's trichrome staining.

Results: CT images were segmented to quantify two volumes: fibrosis (V_F) and lung (V_L). The fraction of these two volumes (V_F/V_T) was calculated in grouped time points (spanning 4 weeks) and tracked upto 26 weeks. Baseline scans were taken of subjects prior to irradiation and subtracted from time point volumes to obtain values analogous to RIPF growth. Significant variance is seen between timepoints and the baseline beginning at 10-12 weeks. 40% of subjects reaching 22 weeks (n=10) developed above average (severe) RIPF. Tidal lung volume (TLV) was also calculated by subtracting expiration scan volumes from inspiration scan volumes. No statistical significance exists; however, the 4 aforementioned severe cases showed little ability to breath during final scanning.

Conclusion: More clincially relevant methodolgy allows for a more clinically relevant model. Pre-clinical studies will be aided by this newly developed model; however, more studies should be done to strengthen the results of this model for future use.

Keywords: Animal Models, Radiation Biology, Computed Tomography, Thoracic Irradiation, Radiation-Induced Pulmonary Fibrosis (RIPF)

Introduction

Thoracic irradiation treatments are among the most common in external beam cancer therapies largely due to the high incidence of breast and lung cancer – the two most prevalent cancers in the world. Lung cancer is the most frequently diagnosed cancer with 1.6 million new cases each year [2] and breast cancer is the second most frequently diagnosed cancer with 1.1 million new cases each year [41,42]. Proving to be an effective treatment, radiation therapy ideally destroys all the cancer's tumor cells while maintaining healthy cells' integrity. However, the ideals prove to be far from realistic with 35% of thoracic irradiation patients at risk to develop lung injury [7–9]. The risk of radiation-induced lung injury, which has limited treatment options, limits the amount of radiation that can be safely delivered to the tumor. Research into the mechanisms and potential therapeutics are usually performed in mouse models that replicate the clinical disease [11,43].

However, current models are problematic in their methodology. Present studies fail to be pertinent in two ways: 1) they fail to accurately replicate clinical methodology for diagnosis and tracking of the disease, and 2) they fail by using mortality as the endpoint. This method of analysis is problematic in pre-clinical studies since clinics do not diagnose patients at their deaths, and instead, image to diagnose and monitor RIPF while the patient is alive. Therefore, there is a critical need to develop a quantifiable paradigm that uses non-invasive imaging to monitor the progression of RIPF usable for comparison in experimental therapeutic studies. It is essential for the model to mimic clinical methodology as much as possible in order to provide more relevant information, so that an experimental treatment's efficacy can be accurately and thoroughly analyzed.

To accomplish this, Computed Tomography (CT) imaging was used to image mice whose lungs were irradiated. From these images, fibrosis was tracked until severe fibrosis was observed or secondary pathology forced the subject to be euthanized. Scans provided data to calculate

volumes of the lung and tissue in the lung. This article reports the volumes found from these scans and tracks them over several weeks to model RIPF's progression. Also, scans were respiratory gated to minimize motion artifacts due to breathing. This gating created two images from each scan – expiration and inspiration. By calculating lung volume for each phase, the difference provides tidal lung volume to provide functional information for the model.

Methods

All animal experiments were approved by the Purdue Animal Care and Use Committee.

Mouse Characteristics

Mice used to develop our model was determined based on previous literature[11]. Forty-three male C57Bl/6 mice were used in this study. Male C57Bl/6 were used due to their reported radioresistance compared to female mice and their historically published pro-RIPF characteristics. Radiosensitivity was of concern because previous trials preformed led to premature death leading to the decision to use mice that were more likely to survive irradiation. Mice were irradiated at 8 weeks-old and weight was not tracked.

Mice were housed in a facility located on Purdue University's campus and maintained by Purdue University's animal care staff. Mice were checked daily by staff and weekly by researcher during imaging dates. Mice that developed severe wounds due to erythema, bullying, or other causes were checked every other day. Euthanasia would be deemed necessary by animal care staff when wounds, after treatment, progressed or remained severe.

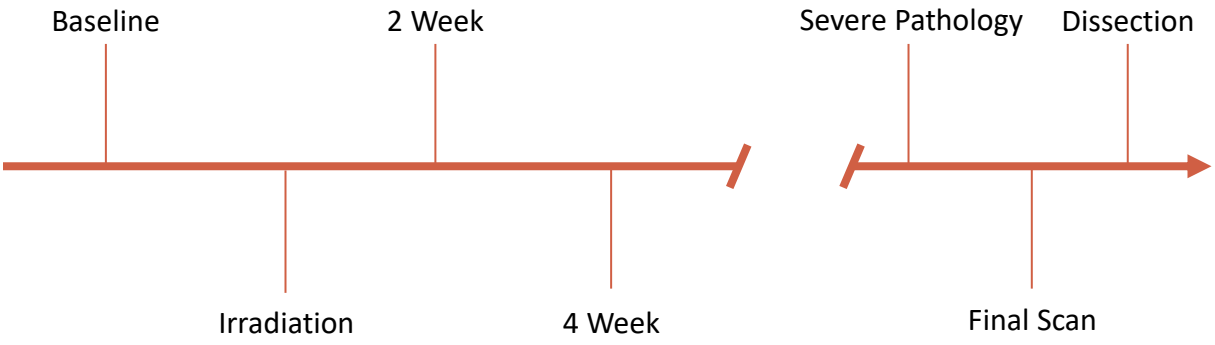

Figure 7: Timeline of experiment. Each subject received a baseline scan before being irradiated. Mice were then scanned subsequent to irradiation every 2 weeks until severe pathology caused premature mortality or required euthanasia.

Irradiations

Mice received a baseline CT scan before irradiations were delivered (**Fig. 1)**. Based on previous studies[11], mice were irradiated with a single fraction dose of 20 Gy to the whole thoracic region with a 320 kV cabinet irradiator (X-Rad 320, Precision X Ray, North Branford, CT). Mice were sedated with Isoflurane in an induction chamber and then kept sedated through a custom-made anesthesia manifold (**Fig. 2a**). Mice were sedated in groups of five and placed on the platform in the prone position with Gafchromic EBT 3 film (Ashland Advanced Materials, Bridgewater NJ) placed beneath for position validation. Lead shielding was then placed above the mice (**Fig. 2b**) with a 7.5 $mm\ x\ 15\ mm$ aperture placed above the thorax of each mouse. Each mouse was adjusted individually to optimize positioning for dose delivery. The cabinet irradiator was set to deliver a dose of 20 Gy with a dose rate of approximately 200 cGy/min (calibrated by another lab) and a tube setting of 320 kV. Source-to-skin distance was set to be 50 cm and a 0.1 mm Al beam-flattening filter was used. Irradiations took approximately 10 minutes to deliver the desired dose given the dose rate. Afterwards, mice were allowed to recover from anesthesia in their cages under observation and returned to the mouse facility.

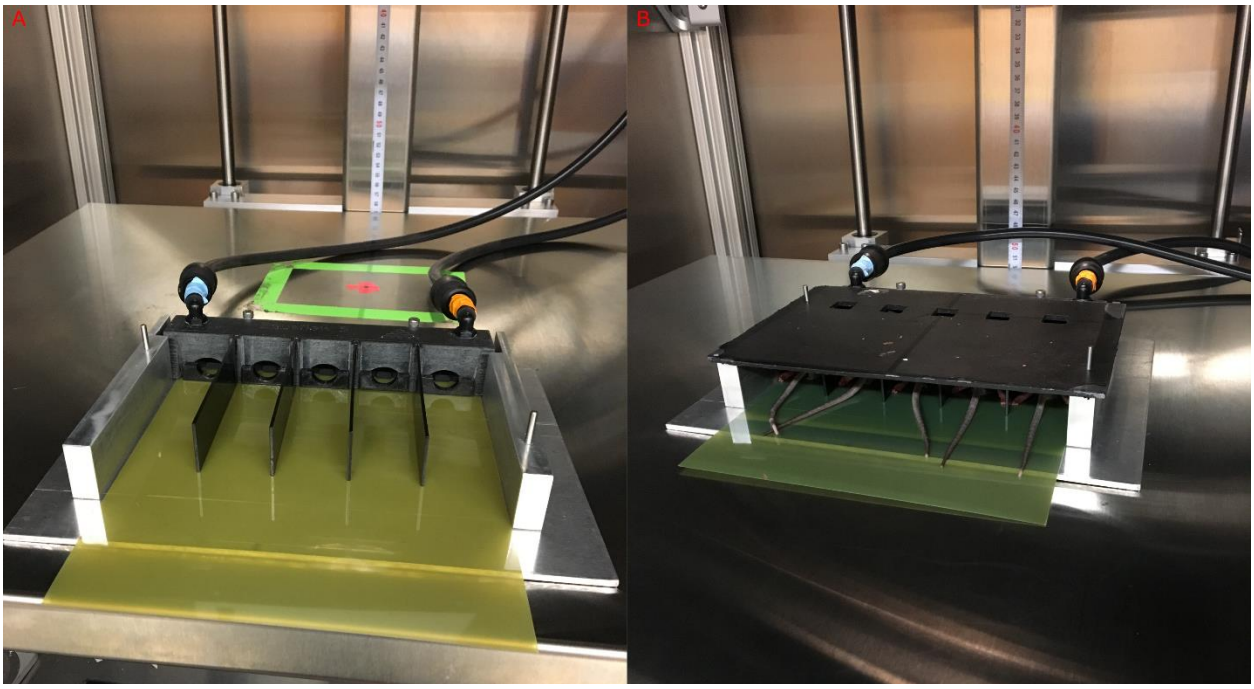

Figure 8: Irradiation setup with **[A]** a 5-chamber platform and attached to a sedative delivery system with a piece of Gafchromic EBT 3 film slid in between the floor of the platform and the mice. **[B]** Mice placed in chambers with lead shielding placed above to contour the x-ray beam to irradiate the thorax of each mouse to deliver 20 Gy to only the lungs.

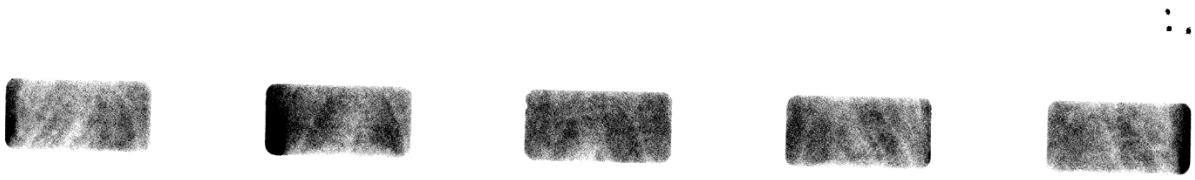

Figure 9: Film of 5 mice's positions relative to the 2.5 $mm\ x\ 5\ mm$ aperture in the lead shielding. It is evident from these films that positioning of the mice lungs are well contoured to adequately irradiate the entirety of the lung.

Film Analysis

Film irradiated during dose delivery was analyzed using an EPSON Perfection V600 photo scanner and the software program ImageJ. After scanning films, the corresponding files were opened with ImageJ where their RGB channels were separated into three individual images. The green channel offered the most contrast for Gafchromic EBT 3 film, so it was used to validate subject positioning during irradiation [44] (**Fig. 3**).

CT Imaging

Mice were imaged using a pre-clinical Perkin-Elmer Quantum Lab GX X-ray microCT in 2 week time points (**Fig. 1**). Mice were anesthetized using isoflurane in order to slow down breathing and make respiratory gating possible and then placed within the bore of the microCT. Images were acquired using respiratory gating and with a 72 mm FOV and then reconstructed with a 36 mm FOV which incurred a dose to the subject of approximately 162 mGy. Images were saved as DICOM files with two separate images produced per scan – expiration and inspiration (**Fig 4**).

Image Segmentation

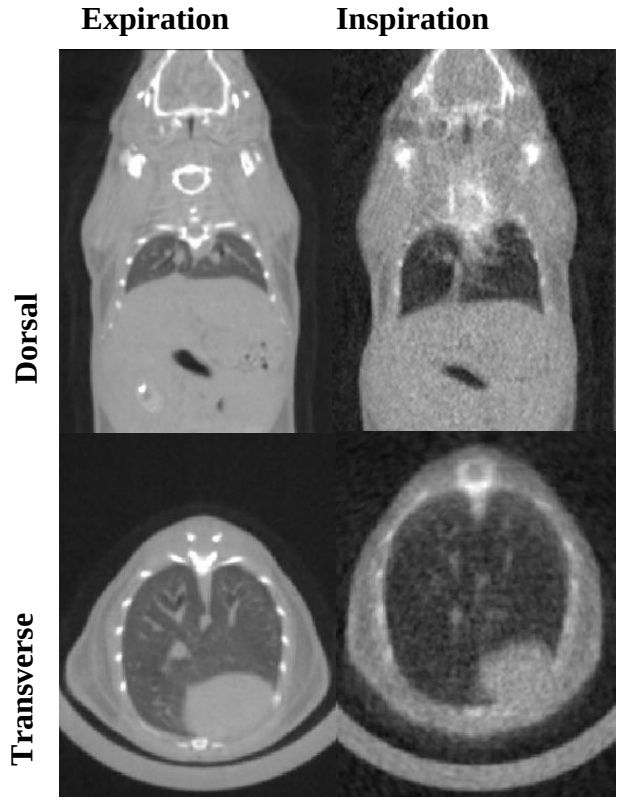

Figure 10: CT images of a baseline scan for the same mouse showing the expiration and inspiration phase in the dorsal and transverse planes.

Images were saved as DICOM files that were compiled using a program called ITK-SNAP. Within this program, images were segmented semi-automatically based off voxel intensity and then manually by hand (**Fig 5a**). After compilation, transverse and dorsal images were cropped to only include areas of the lung. An intensity threshold was set to separate areas of hyperintensity and hypointensity in the lungs. Thresholds were set near -450 HU, since air has an intensity around -600 HU, but adjusted to compensate for possible variations in images. Hypointense areas were filled in as "lung" or air through this semi-automatic segmentation. The segmentation was cleaned up afterwards to best represent only areas in the lung. The trachea was not included in the lung segmentation. Hyperintense areas were filled in manually using a paint brush tool to only fill in areas in the lung unlabeled. Images were checked in all three dimensions for completeness and accuracy. Three dimensional images were generated to show fibrosis and bronchiole pathways (**Fig 5b**).Mice that were euthanized by the researcher were dissected to extract the lungs and heart from the thoracic cavity and placed in 4% paraformaldehyde for preservation and storage. Lungs were then place in 0.05% Agarose to maintain the lungs' structure when sliced. Lungs were sliced along the dorsal plane directly adjacent and dorsal to the heart's apex. Lung slices were placed in 70% ethanol and then embedded in paraffin to generate 4 micron slices. Slices were stained with hematoxylin and eosin and Mason's trichrome and visualized with an Evos-XL light microscope.

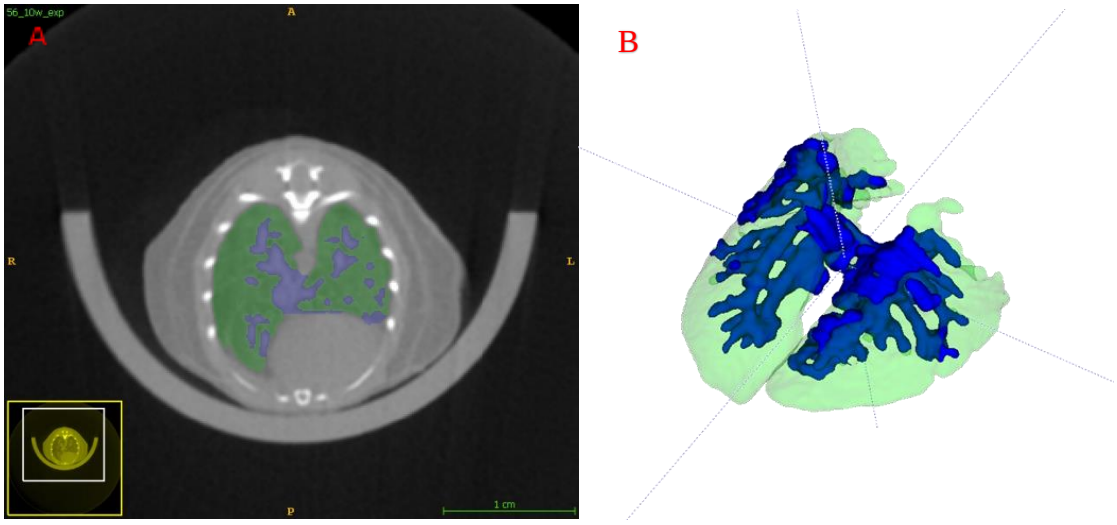

Figure 11: **[A]** Segmentation of CT image in the transverse plane. Segmentations were developed using a semi-automatic algorithm to label areas that were hypointense as "lung." Hyperintense areas were then manually segmented as "fibrosis." **[B]** Three-dimensional construction of segmentation. Areas that are green are "lung" and areas that are blue are "fibrosis."

Results

Hyperintense Signal Fraction and Volumes

Expiration images were used instead of inspiration due to its greater contrast-to-noise ratio (**Fig. 4**) (See *Discussion: Hyperintense Signal*) . Time points were grouped into bins that ranged over 4 weeks (excluding the final time point). This was done to minimize the disparity of sample sizes between time points given the depletion of sample size over time due to mortality.

Figure 6a shows average fractions of hyperintense volumes to total lung volumes (V_F/V_T). Regions segmented from CT images were quantified into volumes (mm^3) to allow for calculations. Volumes segmented as "fibrosis" (V_F) and "lung" (V_L) were summed to find the total lung volume ($V_T = V_F + V_L$) which V_F was divided by to calculate the fraction of fibrosis normalized to lung volumes for each subject at each time point. Given that baseline volumes were not subtracted from this value, the true fraction found was the fraction of hyperintense signal to lung volume (See *Discussion: Hyperintense Signal*). To account for tissue that exists normally in the lungs (e.g. bronchioles), baseline volumes were subtracted from each time point for each subject to calculate any growth of hyperintense signal in CT images over time (**Fig 6b**). This growth would most likely be attributed to RIPF.

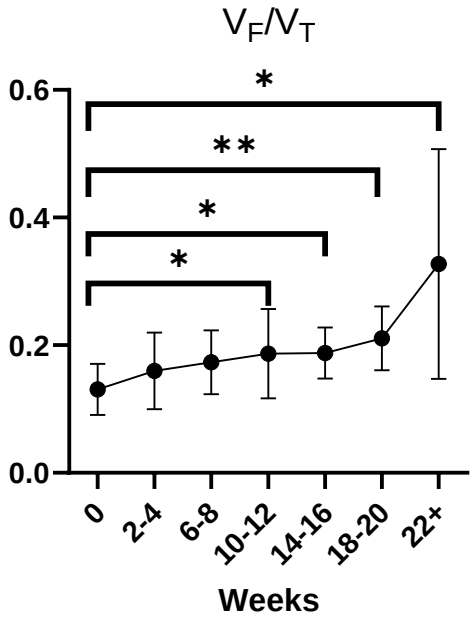

Figure 12: **[A]** Fraction of hyperintense signal (V_F) volume over total lung volume (V_T) with respect to time. Averages slowly increase with an initial plateau until around the 18-20 week time point where averages escalate quickly. **[B]** Average fraction with baseline $(V_F/V_T)_0$ subtracted to determine increase of V_F analogous to fibrosis. Statistically significant deviation from the baseline can be seen beginning at the 10 week time point.

Table 1 shows the average values for each time point group along with the corresponding standard deviation and sample size. Column 2 shows the hyperintense signal fraction while column 6 shows similar statistics for the time points with baseline values subtracted. The data-set for $(V_F/V_T) - (V_F/V_T)_0$ shows smaller sample sizes due to less time points having corresponding baseline values. Significant variance exists among the latest time point and all others. This is discussed further later in the paper (See *Discussion: Average Volumes and Variance*).

Table 1: Column 2 shows averages of hyperintense signal (V_F) volume over total lung volume (V_T) with respect to time points. Column 6 shows the same fraction with the baseline average for the respective time point subtracted. The disparity in sample size between the two averages is due to every subject not having a baseline value available. Column 5 shows the p-value calculated from Dunnett T3 multiple comparisons test between each time point and the baseline.

Weeks	$\boldsymbol{V_F/V_T}$	$\boldsymbol{s}$	$\boldsymbol{N}$	**p-value (vs. B_0)**	$\boldsymbol{(V_F/V_T) - (V_F/V_T)_0}$	$\boldsymbol{s}$	$\boldsymbol{N}$
0	0.1307	0.0385	26		0	0	26
2-4	0.1596	0.0606	21	0.3256	0.0259	0.0862	8
6-8	0.1733	0.0543	9	0.2459	0.0239	0.0621	5
10-12	0.1869	0.0688	15	0.0500	0.0573	0.0487	7
14-16	0.1877	0.0439	9	0.0235	0.0352	0.0463	6
18-20	0.2109	0.0530	11	0.0023	0.0901	0.0443	9
22+	03272	0.1760	10	0.0353	0.2248	0.1854	7

ANOVA

Single-factor Analysis of Variance (ANOVA) was performed on the both data-sets to determine any statistically significant differences between the baseline and time points. Although most time points' standard deviations (s) are equal, the latest time point's is not. For this reason, ordinary ANOVA testing could not be done assuming homogeneous variance , and a Brown-Forsythe and Welch ANOVA test was performed instead. Both tests found significant differences within the timepoints giving p-values of 0.0004 and 0.0002 for V_F/V_T and $(V_F/V_T) - (V_F/V_T)_0$ respectively. This led to completing a multiple comparisons test between each time point and the baseline.

A multiple comparisons test was performed to find statistical significance between time points and the baseline, so a Dunnett's T3 test was performed to find significance since the group sample sizes are all smaller than 50. **Table 1** shows corresponding p-values to time points. Testing was done with a 95% confidence interval ($\alpha \leq 0.05$), so significance can be seen at time points 10-12 weeks and later with the 18-20 week time point being the most significant.

Tidal Lung Volumes

Since CT images were performed using a respiratory gated scan, two images were produced for each subject at each time point – an expiration and inspiration image. These images were segmented and provided volumes for both respiration phases. Subtracting these volumes provided quantized, functional data in tidal lung volume.

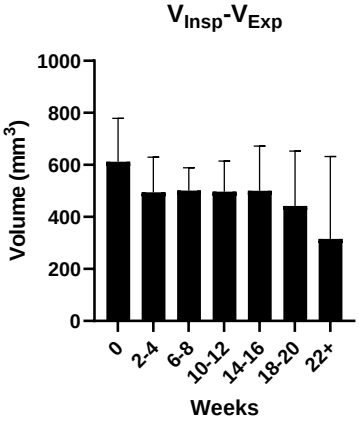

Figure 13: Average tidal lung volume ($V_{Insp} - V_{Exp}$). Despite the decrease of the average over time, no significance exists ($\alpha < 0.05$) between any time points and week 0. This is partially due to the random onset of RIPF at later times as seen in **Fig 8**.

A one-way ANOVA was performed assuming inhomogeneous variances (for similar reasons that the fractions' volumes were inhomogeneous), so a Brown-Forsyth and Welch test were done. Welch's test, the more powerful test of the two, found no significance between all the values, so a multiple comparisons test was not performed afterward. Values from the test can be seen in Table 2.

Table 2: One-way ANOVA test on tidal lung volumes. Welch's ANOVA test was performed on samples with inhomogeneous variance among the compared groups. No significance ($\alpha < 0.05$) was found between any of the time points due to this inhomogeneity and statistically insignificant differences between earlier time points and the baseline.

	Welch's Test	**Brown-Forsyth Test**
$W\ (DF_n, DF_d)$	1.851 (6.000, 24.59)	7.003 (6.000, 20.43)
$p - value$	0.1303	0.0004
Significant diff. among means ($p < 0.05$)?	*No*	*Yes*

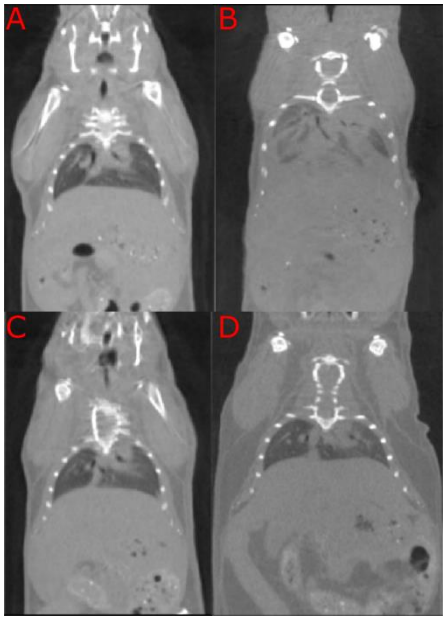

Figure 15: Disparity of severity among late time points. **[A]** Baseline scan of subject 1. **[B]** 26 week scan of subject 1. **[C]** Baseline scan of subject 2. **[D]** 26 week scan of subject 2. Severe RIPF is noticeable in subject 1 at 26 weeks whereas subject 2 has no noticeable signs of RIPF at 26 weeks. All images shown are of the same dorsal slice just dorsal to the heart.

Histology

Histology slides were used to verify presence of fibrosis in euthanized subjects. Mason's Trichrome stains areas blue when there is collagen present. Collagen is a principal constituent of fibrosis.[4,9–11] In **Figure 9**, lung histology shows the alveoli, bronchioles, and blood vessels at 10x magnification. 26 weeks post-irradiation shows scaring primarily around the bronchioles and a greater density of the lung tissue.

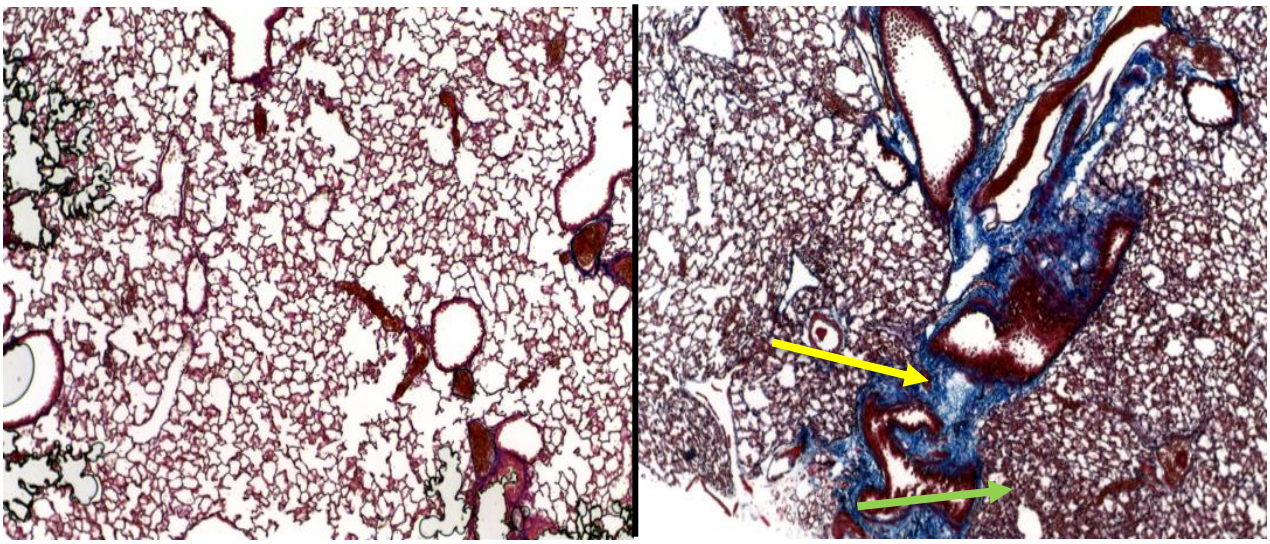

Figure 14: Lung histology with Mason Trichrome stain at 10x magnification. **[L]** Normal lung tissue un-irradiated. **[R]** Lung tissue 26 weeks post-irradiation. Areas of blue on Mason's Trichrome show collagen deposits (yellow arrow) which is a primary constituent of fibrosis. Smaller holes in the lung tissue show the alveoli whereas the larger areas are bronchioles. Fibrotic areas appear primarily around the bronchioles and alveoli appear collapsed (green arrow) in the irradiated lung tissue.

Discussion

Hyperintense Signal

As previously mentioned and seen in **Figure 4**, the expiration image has a much better CNR in comparison to the inspiration image. This is not due to the resolution of the two images, rather, it is due to the number of angles the CT used for image reconstruction. Mice were sedated to minimize lung motion during scanning, but this led to the mice gasping whenever inhaling for air. These quick gasps were when the CT would collect image data for the inspiration phase. The mouse had longer periods where it was not gasping when image data was collected for the expiration phase. This disparity in image angles for image reconstruction and general motion leads to the blurriness and low CNR in the inspiration phase's image.

In using the expiration images for segmentation, hyperintense signals (bright) coming from the lungs are labeled as "fibrosis" whereas hypointense areas (dark) are labeled as "lung." The label of "fibrosis" for the hyperintense signal is a misnomer given that more than fibrosis creates such a signal in the lungs – as evident by the baseline scans containing such signals. Hyperintensity is also caused by tissue in the lungs that make up the air pathways – primarily the bronchioles. As seen in **Fig 5b**, the areas of blue resemble the airways that branch throughout the lung. Over time, these airways still exist; however, they begin to scare (fibrosis) due to the radiation which thickens the tissues and creates greater masses that are seen as hyperintense voxels in the CT image. Given this, the more analogous, experimental quantity to the fibrosis is the volume at a given time point with the subject's baseline volume subtracted away ($V_F(t) - (V_F)_0$).

Average Volumes and Variance

Average V_F/V_T rose throughout the entire timeline although at different rates. Earlier timepoints showed little increase compared to the baseline average. Physiologically, this makes sense given the literature's description of a "latent period" directly after radiation exposure and before RIPF presents physically.[4,8,10,45] Earlier time points create a plateau during this latent period given that fibrosis is a chronic, late-responding injury;[10] meaning that fibrosis takes several weeks for onset and should not appear on CT images.

However, RIPF severity and onset did not consistently appear in subjects. **Figure 7b** shows severe RIPF at 26 weeks – to the point of no respiration – whereas **Figure 7d** shows a different

subject at the same time point. **Figures 7a** and **7c** provide the baseline images for comparison. This disparity between subjects of RIPF development created large variance for later time points especially at 22+ weeks.

Table 3: This table shows averages of hyperintense signal fraction (V_F/V_T) and (V_F/V_T)- $(V_F/V_T)_0$ along with their corresponding 95% confidence intervals. Intervals appear much wider for later time points due RIPF's severity disparity and for $(V_F/V_T) - (V_F/V_T)_0$ due time points' smaller sample sizes.

Weeks	$\boldsymbol{V_F/V_T}$	**95% C.I.**	$\boldsymbol{(V_F/V_T) - (V_F/V_T)_0}$	**95% C.I.**
0	0.1307	$(0.1301 - 0.1313)$	0	
2-4	0.1596	$(0.1581 - 0.1612)$	0.0259	$(0.0207 - 0.0310)$
6-8	0.1733	$(0.1714 - 0.1752)$	0.0239	$(0.0205 - 0.0272)$
10-12	0.1869	$(0.1845 - 0.1893)$	0.0573	$(0.0556 - 0.0591)$
14-16	0.1877	$(0.1865 - 0.1890)$	0.0352	$(0.0335 - 0.0369)$
18-20	0.2109	$(0.2092 - 0.2125)$	0.0901	$(0.0888 - 0.1914)$
22+	0.3272	$(0.3080 - 0.3464)$	0.2248	$(0.1993 - 0.2502)$

$(V_F/V_T)_0$ had the least amount of variance in its sample distribution due to the large sample size. Although there was a wide range in the distribution $(0.074 - 0.197)$ of $(V_F/V_T)_0$, the large sample size (n=26) creates the greatest confidence in the sample mean adequately representing the population mean. Later time points' distributions are less normal due to decreased sample sizes thus creating wider confidence intervals **(Table 3)**. This greater variation creates greater uncertainty of the population mean leading to less powerful tests to compare time points. However, significance can still be determined despite the smaller sample sizes (See *Discussion: ANOVA and Statistical Significance*). The reason for this great variance at later time points is primarily due to subjects, post-irradiation, exhibited secondary pathologies, such as erythema, from the radiation that led to premature mortality or euthanasia. Almost half of the subjects were unable to make it pass the 12 week time point. Of the 43 subjects used in this study, 25 were still alive 12 weeks post-irradiation (58%) and only 9 subjects made it to 22 weeks (21%).

Tidal Lung Volume

Tidal Lung Volume (TLV) is the volume of air distributed during normal respiration in one cycle. Although mice may be distressed during anesthetization, enough time had passed before scanning that mice were in a more relaxed breathing sequence.

Calculating TLV from CT images provided functional information related to the mice's ability and capacity to breathe. Presumably, TLV would decrease as RIPF increased; however, no discernable conclusions could be made from our data given the significant variance that existed within later time points (see *Discussion: ANOVA and Statistical Significance*).

Histology

Histological slides were a means to validate the presence of fibrosis in subjects whose remains were able to be autopsied. All subjects showed presence of significant collagen deposits in the lungs (**Fig 9**); however, thorough analysis of these slides was unable to be completed in this study and is the next step in further validating our findings.

ANOVA and Statistical Significance

Although the 22+ week time point showed greatest deviation from the baseline average, its large variance created greater uncertainty in the sample's representation of the population. This variance can be attributed to the variation of RIPF's onset and severity; becoming more varying at the later time points. For example, one subject at 26 weeks shows severe RIPF in contrast to another subject at the same time point (**Fig 7**). This difference is a sample of what caused the great variance at the 22+ week time point. Furthermore, the small sample size at 22+ week due to premature mortality aided in the greater variance along with severity disparity. Of the 10 subjects able to make it 22+ weeks, 3 subjects had significantly higher V_F/V_T than the average $\overline{V_F/V_T}_{22} = 0.3272$: $0.4400, 0.5763,$ and 0.6655. These subjects had severe cases of RIPF as opposed to the other 7 subjects that had less severe RIPF. Qualitatively, severe cases can be discerned when almost half the lung appears fibrotic (**Fig 8b**).

To analyze the variance (ANOVA) of V_F/V_T, Welch's and Brown-Forsyth's tests were performed since there is inhomogeneity among the variances and sample sizes of the time points. V_F/V_T is also preferable over $V_F/V_T - (V_F/V_T)_0$ for analysis due to the larger sample sizes at each respective time point. Welch's test holds more power over Brown-Forsyth's test unless distributions are not Gaussian, so its test statistic is more trustworthy in this case. Welch's test statistic for V_F/V_T was $W_{6.000,31.98} = 6.132$ with a p-value of $p = 0.0002$. Given our confidence interval of 95% ($\alpha = 0.05$), this shows there is great significance between all the time points.

Given the previously stated Dunnett's T3 multiple comparisons test (**Table 1** and **Fig 6b**), significant deviations from $(V_F/V_T)_0$ can be seen beginning at 10-12 weeks. This means that most cases of RIPF in mice will begin being detected by CT around 10-12 weeks.

Another ANOVA was performed again using Welch's test on the mice's tidal lung volumes. Welch's test statistic produced $W_{6.000,24.59} = 1.851$ with a p-value of $p = 0.1303$. This time the test showed no significant differences between the time points' average tidal lung volumes. This is surprising given that the 3 subjects at 22+ weeks with larger V_F/V_T than the average were barely able to breathe during final scanning. Their RIPF was so severe that their diaphragms were unable to contract significantly enough for the respiratory gating to distinguish between the expiration and inspiration phases – there was only one image reconstructed. However, the large variance in these values factors into the test as a penalty thus outputting a larger W-statistic and p-value. More than likely, a larger sample size would have generated greater significance between the time points.

Conclusions and Future Directions

The model presented in this paper was a more relevant, clinical model for future RIPF studies. We were able to better track and quantify RIPF's progression beyond mortality rates by using diagnostic tools analogous to clinics' methods for tracking RIPF patients. This model will benefit future pre-clinical studies to recognize the effectiveness of any treatment given to mice.

Further studies should be done to strengthen this model. As previously stated, histology slides should be analyzed and map areas of fibrosis to corresponding subjects' CT images for spatial validation.

A similar study should also be done that is able to better prevent premature mortalities and provide larger sample sizes at later time points. This would create greater confidence in sample averages representing population means and generate more powerful ANOVA tests.

Our irradiation set-up poorly resembles the clinic since our irradiations are high, single-fraction doses. A multi-fractionated irradiation would be the next logical step in developing a more clinically relevant model.

With RIPF being such a permanent and severe injury caused to those who are already dealing with a serious cancer diagnosis, it's important to take the next steps in finding a treatment to minimize RIPF occurrence and prevent cancer survivors from facing further injury, so they can live a normal life.

CHAPTER 3: COMPARISON OF CT AND MR IMAGED MURINE RADIATION-INDUCE PULMONARY FIBROSIS (RIPF) FROM WHOLE THORACIC IRRADIATION

Daniel R. McIlrath, MS[1], and Carlos J. Perez-Torres, PhD[1,2*].

[1]*School of Health Sciences, Purdue University, West Lafayette, Indiana, US*

[2]*Purdue University Center for Cancer Research, Purdue University, West Lafayette, Indiana, US*

[1]Address for correspondence: School of Health Sciences, Purdue University, 550 Stadium Mall Drive, Hampton Hall 1263A, West Lafayette, IN 47907, USA; cperezto@purdue.edu

Abstract

Background: Mouse models of radiation-induced lung fibrosis (RIPF) are commonly produced to find novel treatments for the condition. However, current use solely CT as the imaging modality to detect RIPF. With greater tissue contrast and ionizing radiation sparing, MRI offers great benefits to any radiation model. However, MRI images the lungs poorly due to air producing quickly decaying, undetectable signals even in extremely high magnetic fields. A new scan sequence called ultra-short TE (UTE) though overcomes this hurrdle by shortening TE to under $0.5\ ms$.

Methods: Male C57Bl/6 mice (n=7) were irradiated with a single dose of 20 Gy to the whole thoracic area delivered by an 320 kV X-Rad cabient irradiator. CT was performed with respitory gating at 0, 5, and 8 week timepoints and developd images to identify RIPF pathology *in vivo*. This process was repeated with MRI at the same time points.

Results: CT and MR images were segmented to quantify two volumes: fibrosis (V_F) and lung (V_L). The fraction of these two volumes (V_F/V_T) was calculated at each time point and compared. Significant difference is seen between timepoints and the baseline for the MRI scans but not the CT. Comparison between the two modalities shows no evidence to differentiate between the two modalities' results. However, MRI fails to show RIPF severity when compared to an 8-week time point CT scan taken within 24 hours of another.

Conclusion: Concern is raised of MRI's ability to accurately detect RIPF within the lungs. With using CT as a basis for RIPF's development, MRI fails to match its increase in variance over time. Failing to replicate CT's results, MRI needs more adjustments for it be closer to CT's contrast ability. Still, pre-clinical studies will be aided by this new methodology and the potential it holds; however, more studies should be done to strengthen the contrast and resolution of the MR image.

Keywords: Animal Models, Radiation Biology, Computed Tomography, Magnetic Resonance Imaging, Thoracic Irradiation, Radiation-Induced Pulmonary Fibrosis (RIPF)

Introduction

Thoracic irradiation treatments are among the most common in external beam cancer therapies largely due to the high incidence of breast and lung cancer – the two most prevalent cancers in the world. Lung cancer is the most frequently diagnosed cancer with 1.6 million new cases each year [2] and breast cancer is the second most frequently diagnosed cancer with 1.1 million new cases each year [41,42]. Proving to be an effective treatment, radiation therapy ideally destroys all the cancer's tumor cells while maintaining healthy cells' integrity. However, the ideals prove to be far from realistic with 35% of thoracic irradiation patients at risk to develop lung injury [7–9]. The risk of radiation-induced lung injury, which has limited treatment options, limits the amount of radiation that can be safely delivered to the tumor. Research into the mechanisms and potential therapeutics are usually performed in mouse models that replicate the clinical disease [11,43].

However, current models are problematic in their methodology. Present studies fail to be pertinent in two ways: 1) they fail to accurately replicate clinical methodology for diagnosis and tracking of the disease, and 2) they fail by using mortality as the endpoint. This method of analysis is problematic in pre-clinical studies since clinics do not diagnose patients at their deaths, and instead, image to diagnose and monitor RIPF while the patient is alive. Therefore, there is a critical need to develop a quantifiable paradigm that uses non-invasive imaging to monitor the progression of RIPF usable for comparison in experimental therapeutic studies. It is essential for the model to mimic clinical methodology as much as possible in order to provide more relevant information, so that an experimental treatment's efficacy can be accurately and thoroughly analyzed.

To accomplish this, Computed Tomography (CT) imaging was used to image mice whose lungs were irradiated. From these images, fibrosis was tracked until severe fibrosis was observed or secondary pathology forced the subject to be euthanized. Scans provided data to calculate volumes of the lung and tissue in the lung. This article reports the volumes found from these scans and tracks them over several weeks to model RIPF's progression. Also, scans were respiratory gated to minimize motion artifacts due to breathing. This gating created two images from each scan – expiration and inspiration. By calculating lung volume for each phase, the difference provides tidal lung volume to provide functional information for the model.

Methods

All animal experiments were approved by the Purdue Animal Care and Use Committee.

Mouse Characteristics

Mice used to develop our model was determined based on previous literature[11]. Seven male C57Bl/6 mice were used in this study. Male C57Bl/6 were used due to their reported radioresistance compared to female mice and their historically published pro-RIPF characteristics. Radiosensitivity was of concern because previous trials preformed led to premature death leading to the decision to use mice that were more likely to survive irradiation. Mice were irradiated at 8 weeks-old and weight was not tracked.

Mice were housed in a facility located on Purdue University's campus and maintained by Purdue University's animal care staff. Mice were checked daily by staff and weekly by researcher during imaging dates. Mice that developed severe wounds due to erythema, bullying, or other causes were checked every other day. Euthanasia would be deemed necessary by animal care staff when wounds, after treatment, progressed or remained severe.

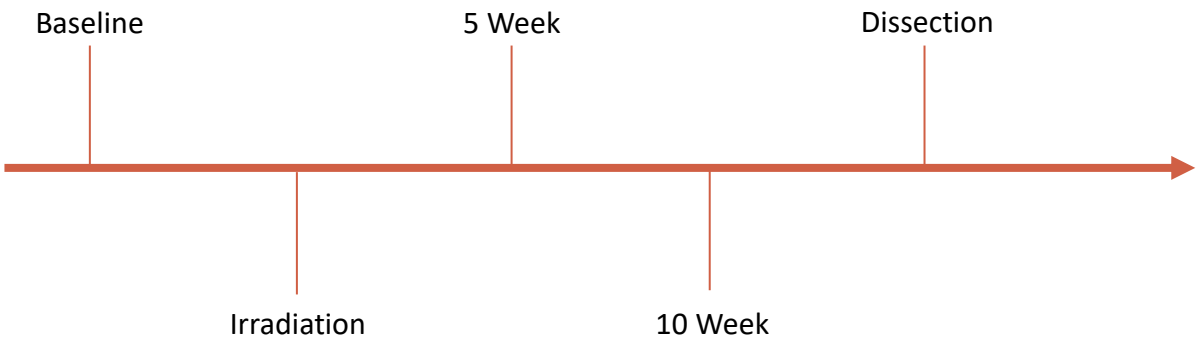

Figure 16: Timeline of experiment. Each subject received a baseline scan before being irradiated. Mice were then scanned subsequent to irradiation at 5 and 10 weeks and then euthanasia.

Irradiations

Mice received a baseline CT scan before irradiations were delivered **(Fig. 10)**. Based on previous studies[11], mice were irradiated with a single fraction dose of 20 Gy to the whole thoracic region with a 320 kV cabinet irradiator (X-Rad 320, Precision X Ray, North Branford, CT). Mice were sedated with Isoflurane in an induction chamber and then kept sedated through a custom-made anesthesia manifold (**Fig. 11a**). Mice were sedated in groups of five and placed on the platform in the prone position with Gafchromic EBT 3 film (Ashland Advanced Materials, Bridgewater NJ) placed beneath for position validation. Lead shielding was then placed above the mice (**Fig. 11b**) with a 7.5 $mm\ x\ 15\ mm$ aperture placed above the thorax of each mouse. Each mouse was adjusted individually to optimize positioning for dose delivery. The cabinet irradiator was set to deliver a dose of 20 Gy with a dose rate of approximately 200 cGy/min (calibrated by another lab) and a tube setting of 320 kV. Source-to-skin distance was set to be 50 cm and a 0.1 mm Al beam-flattening filter was used. Irradiations took approximately 10 minutes to deliver the desired dose given the dose rate. Afterwards, mice were allowed to recover from anesthesia in their cages under observation and returned to the mouse facility.

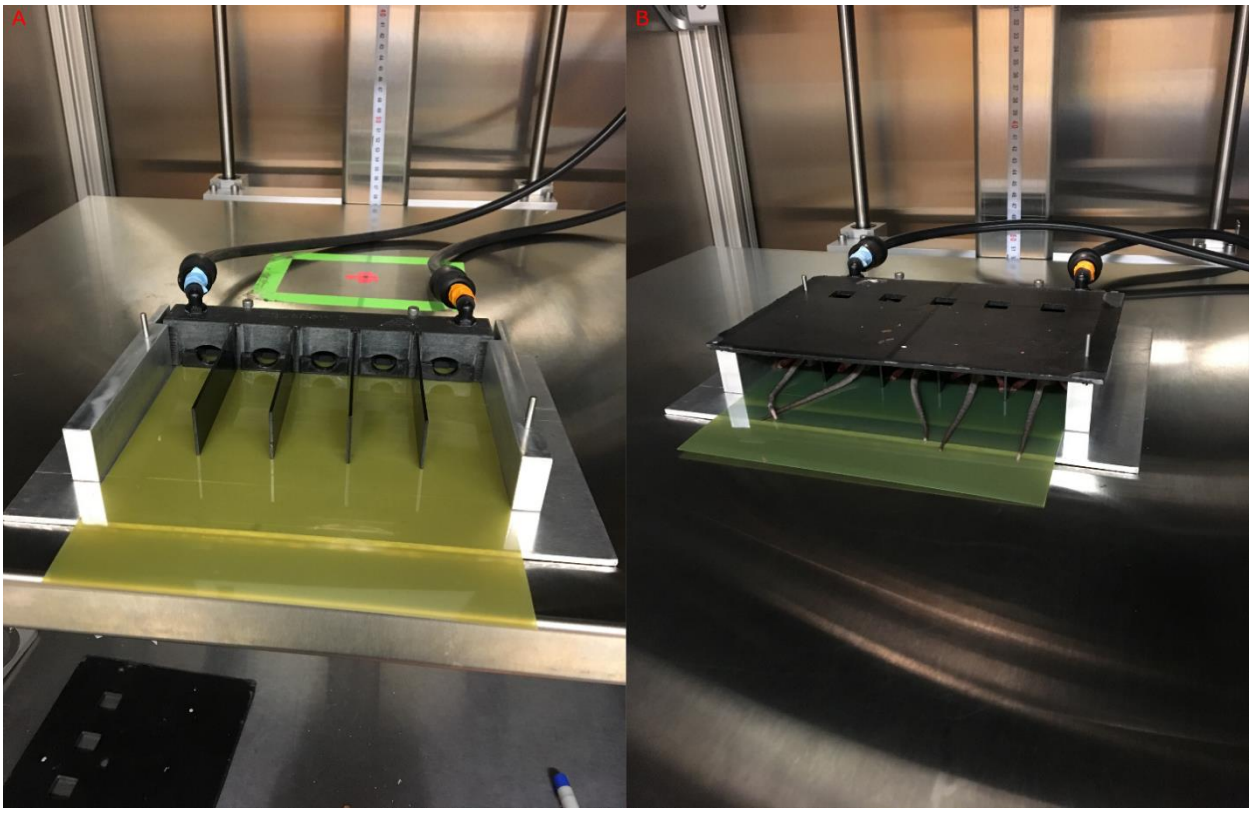

Figure 17: Irradiation setup with **[A]** a 5-chamber platform and attached to a sedative delivery system with a piece of Gafchromic EBT 3 film slid in between the floor of the platform and the mice. **[B]** Mice placed in chambers with lead shielding placed above to contour the x-ray beam to irradiate the thorax of each mouse to deliver 20 Gy to only the lungs.

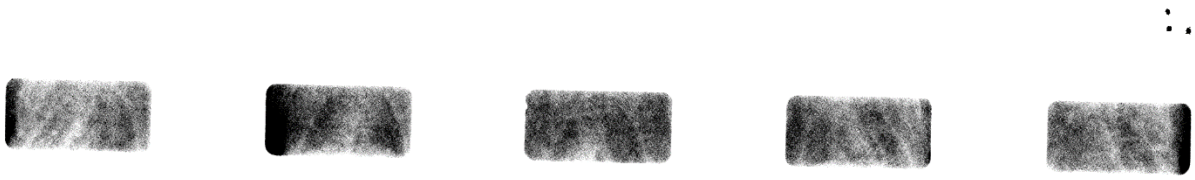

Figure 18: Film of 5 mice's positions relative to the 2.5 $mm\ x\ 5\ mm$ aperture in the lead shielding. It is evident from these films that positioning of the mice lungs are well contoured to adequately irradiate the entirety of the lung.

Film Analysis

Film irradiated during dose delivery was analyzed using an EPSON Perfection V600 photo scanner and the software program ImageJ. After scanning films, the corresponding files were opened with ImageJ where their RGB channels were separated into three individual images. The green channel offered the most contrast for Gafchromic EBT 3 film, so it was used to validate subject positioning during irradiation [44] (**Fig. 12**).

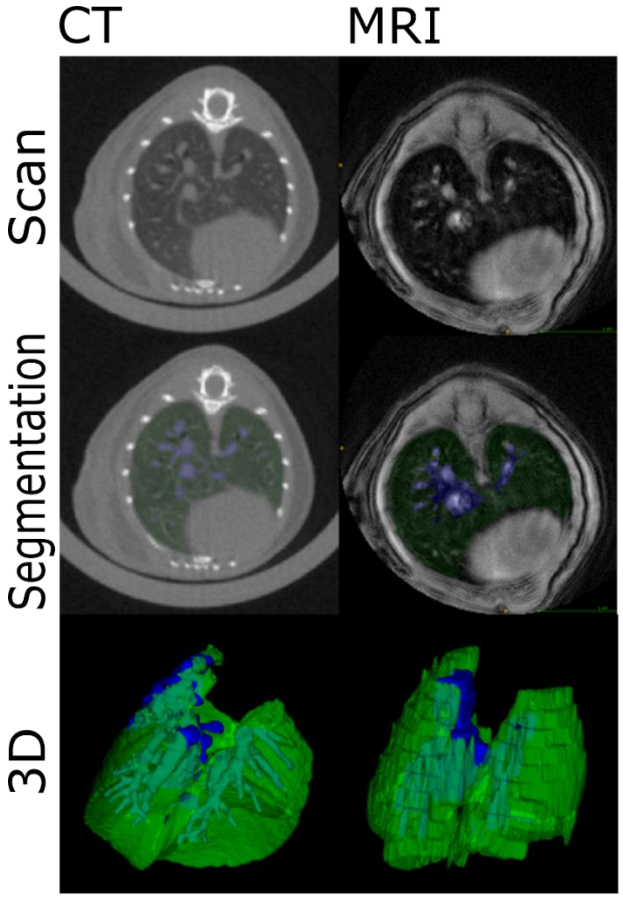

Figure 19: CT and MR scan images, segmentations, and 3D reconstructions. CT shows much greater CNR compared to MRI as well as resolution as can be seen especially in the blocky 3D reconstruction. MR images have worse resolution due to acquiring the scan axially with 1 mm thickness.

CT Imaging

Mice were imaged using a pre-clinical Perkin-Elmer Quantum Lab GX X-ray microCT at three different time points: 0, 5, and 8 weeks (**Fig. 10**). (Mice had to be imaged earlier due to erythema and self-inflicted wounds on the subjects forcing euthanasia). Mice were anesthetized using isoflurane in order to slow down breathing and make respiratory gating possible and then placed within the bore of the microCT. Images were acquired using respiratory gating and with a 72 mm FOV and then reconstructed with a 36 mm FOV which incurred a dose to the subject of approximately 162 mGy. Images were saved as DICOM files with two separate images produced per scan – expiration and inspiration.

MRI

Mice were imaged using a Bruker 7T BioSpec 70/30USR pre-clinical MRI using an Ultra-short TE (UTE) scan. Mice were imaged with axial slices that were approximately 1.0 mm thick

with a field-of-view of 25 mm x 25 mm and 256 x 256 resolution. UTE parameters were set to have a TE= 0.4 ms and TR= 8 ms with 4 averages taken using a 40 mm TR volume coil. Motion was minimized by using a breathing pad to trigger signal acquisition and by athetizing mice with Isoflurane to slow breathing. Images were saved as DICOM files.

Image Segmentation

Images saved as DICOM files were compiled using a program called ITK-SNAP. Within this program, images were segmented semi-automatically based off voxel intensity and then manually by hand. Both CT and MR images were able to be segmented this way (**Fig 13**). CT expiration images were used instead of inspiration due to its greater signal-to-noise ratio. After compilation, transverse and dorsal images were cropped to only include areas of the lung. An intensity threshold was set to separate areas of hyperintensity and hypointensity in the lungs. Thresholds were set near -450 HU for CT, since air has an intensity around -600 HU, but adjusted to compensate for possible variations in images. Thresholds for MRI, which have a different scale than CT, were around 6000 (See *Discussion: CT, MRI Averages and Variance*). Hypointense areas were filled in as "lung" (V_L) or air through this semi-automatic segmentation. The segmentation was cleaned up afterwards to best represent only areas in the lung. The trachea was not included in the lung segmentation. Hyperintense areas were filled in manually using a paint brush tool to only fill in areas in the lung unlabeled. These areas were labeled as "fibrosis"

Table 4: Average fraction of hyperintense signal (V_F) to total lung volume (V_T) for CT and MRI time points. Along with the average value is the standard deviation and the adjusted p-value from Dunnett's T3 multiple comparison's test. Significant differences from the baseline is only seen at MRI's 8 week time point.

$$V_F/V_T$$

	0 Weeks		5 Weeks		8 Weeks	
Mouse	*CT*	*MRI*	*CT*	*MRI*	*CT*	*MRI*
1	0.1251	0.1086	0.1158	0.1005	0.0934	0.1715
2	0.1079	0.1387	0.0770	0.0749	0.1027	0.2247
3	0.0583	0.0620	0.1001	0.2232	0.1093	0.2379
4	0.1362	0.1280	0.2138	0.2135	0.1091	0.2806
5	0.1506	0.0863	0.0615	0.1508	0.4144	-
6	0.0947	0.1143	0.1554	0.1708	0.1429	0.2617
7	0.1007	0.0960	0.1276	0.2197	0.4618	0.2338

(V_F). Images were checked in all three dimensions for completeness and accuracy. Three dimensional images were generated to show fibrosis and bronchiole pathways (**Fig 13**).

Results

CT and MRI Data

Segmented volumes were used to calculate fractions of fibrosis to total lung volume. Volumes V_F and V_L were used to find the total lung volume through their sum: $V_T = V_F + V_L$. The total lung volume was used as the normalization value for each subject to find the fraction of fibrosis in each lung (V_F/V_T).

Table 4 shows fibrosis fractions for each subject at the three time points. Only one data point is missing due to pre-mature mortality after its CT scan, presumably due to severe RIPF.

CT and MRI Averages

Table 5 shows the averages of V_F/V_T for CT and MRI segmented images. Along with the average values are the standard deviations and adjusted p-values obtained from the Dunnett's T3 multiple comparisons test. Variance for both CT and MRI time points are homogeneous except for

CT's 8 week time point. Both CT and MRI averages show an increase in V_F/V_T over time but only the MRI data shows significant difference between the baseline value and suceeding time points.

Single-factor Analysis of Variance (ANOVA) was performed on the both data-sets of V_F/V_T to determine any statistically significant differences between the baseline and time points. Although most time points' standard deviations (S.D.) are equal, the latest time point's is not. For this reason, ordinary ANOVA testing could not be performed assuming homogeneous variance , and a Brown-Forsythe and Welch ANOVA test was performed instead. Welch's ANOVA tests found significant differences within the timepoints for only the MRI average giving adjusted p-values of 0.3550 and 0.0001 for CT and MRI respectively. After performing the ANOVA tests, a multiple comparisons test between each time point and the baseline was performed for both CT and MRI.

A Dunnett's T3 multiple comparisons test was performed to find significance between time points since the group sample sizes are all smaller than 50. **Table 2** shows corresponding p-values to time points for both CT and MRI. Testing was done with a 95% confidence interval

Table 5: Average fraction of hyperintense signal (V_F) to total lung volume (V_T) for CT and MRI time points. Along with the average value is the standard deviation and the adjusted p-value from Dunnett's T3 multiple comparison's test. Significant differences from the baseline is only seen at MRI's 8 week time point.

	CT V_F/V_T			**MRI V_F/V_T**		
	Average	**S.D.**	**p-value (vs. B_0)**	**Average**	**S.D.**	**p-value (vs. B_0)**
Baseline	0.1105	0.0304	-	0.1049	0.0290	-
5 Weeks	0.1216	0.0513	0.8589	0.1648	0.0595	0.076
8 Weeks	0.2048	0.1607	0.3084	0.2351	0.0373	0.0001

Table 6: Dunnett's T3 Multiple Comparison Test between CT and MRI. Average difference between time points is show as well as the 95% confidence interval and adjusted p-value for each comparison. Large p-values heavily suggest equivalent population means between the two groups. Baseline and 8 week time points show significant similarities while the 5 week time point shows a less equivalent comparison.

	Mean Diff.	95.00% CI of diff.	Adjusted P Value
0 Weeks MRI vs. 0 Weeks CT	-0.00563	-0.05293 to 0.04167	0.9744
5 Weeks MRI vs. 5 Weeks CT	0.04318	-0.04968 to 0.1360	0.4125
8 Weeks MRI vs. 8 Weeks CT	0.03025	-0.1934 to 0.2539	0.9462

($\alpha \leq 0.05$), so significance is seen only in the MRI set of timepoints with 8 weeks showing the most significance.

CT vs. MRI

After averages were calculated for each time point for CT and MRI, a one-way ANOVA was performed to determine any significant differences between population mean in each group. After the ANOVA, a Dunnett's multiple comparisons test was ran to compare CT and MRI data sets to each other at respective time points. **Table 6** shows the mean difference, 95% confidence interval, and adjusted p-value from the multiple comparisons test. High adjusted p-values were found for baseline values and at 8 weeks. However, 5 weeks showed a much smaller value for its adjusted p-value. Week 5 also shows the greatest mean difference between the two data sets albeit by 0.01 larger than the 8 week time point's mean difference.

Discussion

CT, MRI Averages and Variance

As previously mentioned, the expiration image has a much better SNR in comparison to the inspiration image. This is not due to the resolution of the two images, rather, it is due to the number of angles the CT used for image reconstruction. Mice were sedated to minimize lung motion during scanning, but this led to the mice gasping whenever inhaling for air. These quick gasps were when the CT would collect image data for the inspiration phase. The mouse had longer periods where it was not gasping when image data was collected for the expiration phase. This disparity in data collection for image reconstruction and general motion leads to the low SNR in the inspiration phase's image.

In using the expiration images for segmentation, hyperintense signals (bright) coming from the lungs are labeled as "fibrosis" whereas hypointense areas (dark) are labeled as "lung." The label of "fibrosis" for the hyperintense signal is a misnomer given that more than fibrosis creates such a signal in the lungs – as evident by the baseline scans containing such signals.

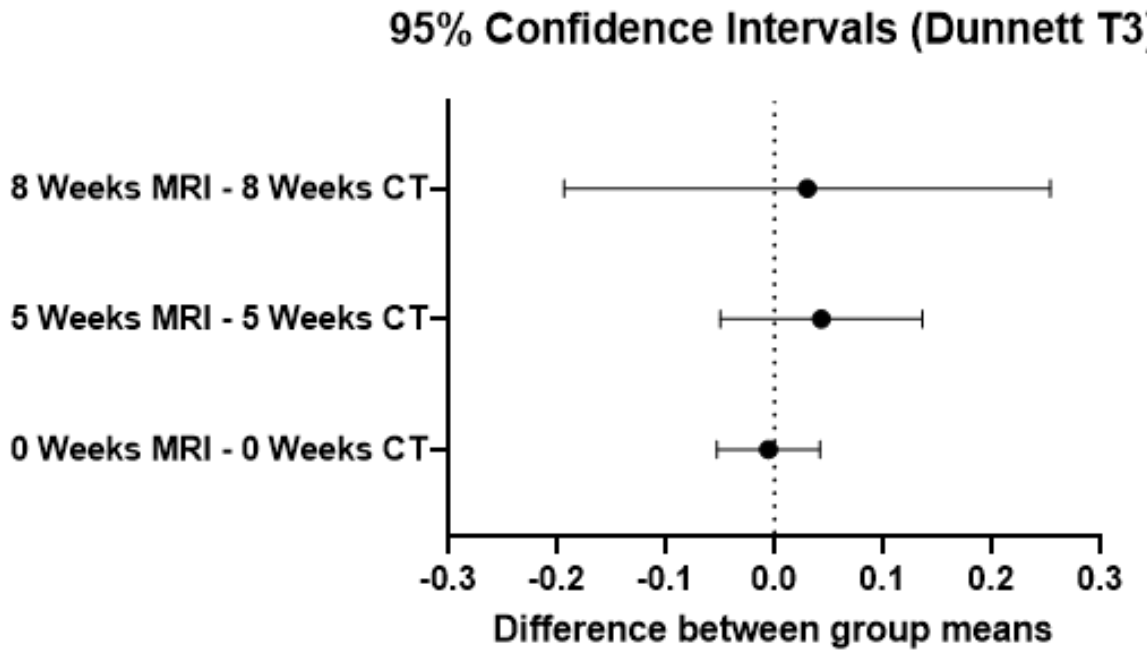

Figure 20: 95% confidence intervals from the Dunnett's T3 multiple comparisons test. The central value shows the mean difference between the two sample group averages and the error bars span the 95% confidence interval for those mean differences.

Hyperintensity is also caused by tissue in the lungs that make up the air pathways – primarily the bronchioles. As seen in **Fig 4** in the 3D reconstruction, the areas of blue resemble the airways that branch throughout the lung. Over time, these airways still exist; however, they begin to scar (fibrosis) due to the radiation which thickens the tissues and creates greater masses that are seen as hyperintense voxels in the CT image. Given this, the more analogous, experimental quantity to the fibrosis is the volume at a given time point with the subject's baseline volume subtracted away ($V_F(t) - (V_F)_0$). However, since the purpose of this article is to compare values to the baseline and between CT and MRI and not attempt to quantify RIPF, it was not necessary to calculate this quantity.

MR images were analyzed in a similar manner except the threshold for the automatic segmentation was different. CT image intensity values are based on Hounsfield units – an objective

standard relating recorded linear attenuation coefficients (μ) to water's μ. MRI intensity in the DICOM images is more complicated since the value is dependent on many factors. For spin echo sequences, signal intensity is typical determined by:

$$S = K[H]\left(1 - e^{-\frac{TR}{T1}}\right)e^{-\frac{TE}{T2}}$$

Where K is a scaling constant, and [H] is the proton density.[18]

Both CT and MRI averages V_F/V_T increased across the three time points (**Table 2**), but MRI showed more significant differences than CT. The primary reason for this is due to the variance of the 8 week time points – CT shows a greater variance than MRI. In a previous study, studying RIPF quantification using CT images, a larger sample size of CT images showed a significant difference of V_F/V_T from V_F/V_{T_0} beginning around the 10-12 week time point and later. This indicates that the small sample size accounts for the lack of significance between time points.

It causes concern that the variance among MRI averages does not reflect the disparity seen in CT at later time points. The inhomogeneous variance is attributed to a disparity in the progress of RIPF – later time points show greater variance in severity due to the variability of RIPF's onset. MRI's data does not reflect this occurrence that was previously observed. Of the mice at the 8 week time point (n=7), 2 subjects showed significantly greater values for V_F/V_T than the average (0.4145, 0.4618). These values were not seen by the MRI.

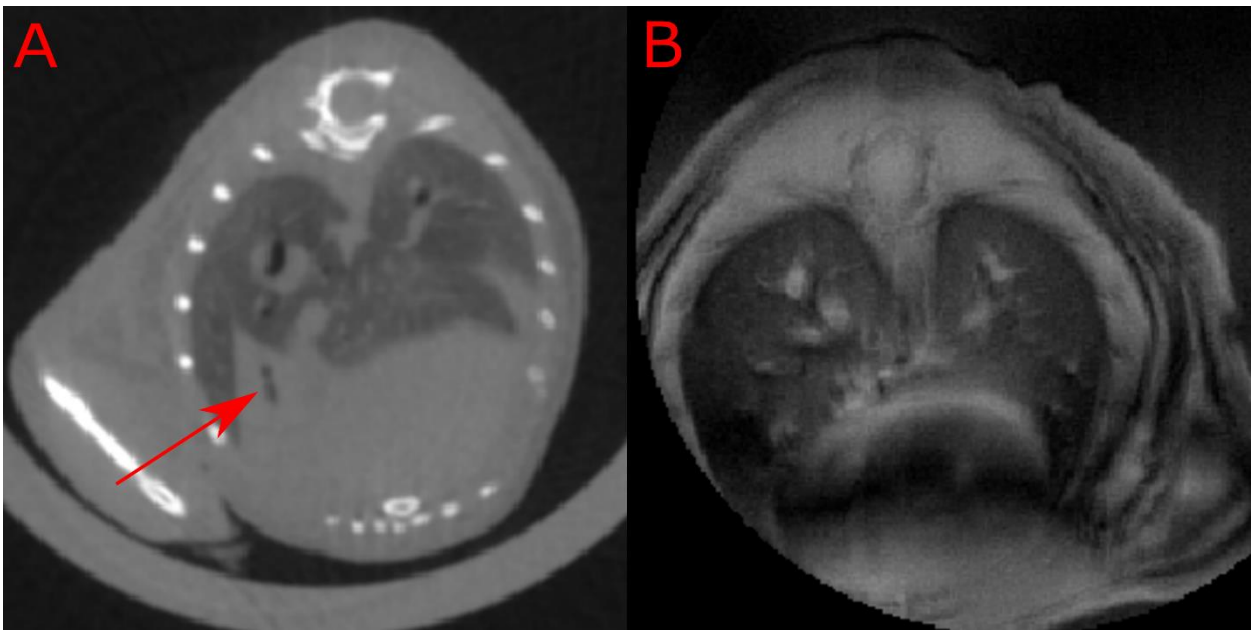

Figure 21: Comparison of subject 180's CT (A) and MR (B) images taken at 8 weeks. Noticeable RIPF is seen in the CT image especially near the heart (red arrow), but the MR image fails to produce any noticeable pathology in comparison.

CT vs. MRI

To analyze the variance (ANOVA) of V_F/V_T between CT and MRI, Welch's and Brown-Forsyth's tests were performed since there is inhomogeneity among the variances and sample sizes of the time points. Given that all groups of time points for CT and MRI were being analyzed in this test, its result does not provide applicable information since we know there is statistically significant differences between MRI's time points. What is of more concern is the Dunnett's T3 multiple comparisons test performed post ANOVA. This compared CT with MRI at respective time points to determine if any significant difference between population means exists.

Table 6 shows the mean difference between the CT and MRI average V_F/V_T and the corresponding 95% confidence interval and adjusted p-value calculated from Dunnett's T3 multiple comparisons test. Since multiple comparisons were made, a correction had to be made to compensate for possible error. This was done by using the Dunnett's T3 test that corrects for multiple comparisons at the expense of the test's power.[46]

Baseline and 8 week values show large adjusted p-values: 0.9744 and 0.9462 respectively. This means that there is at least a 95% chance that the population means between the CT and MRI

averages are the same at 0 and 8 weeks. At 5 weeks, the adjusted p-value is significantly smaller indicating a less than 50% chance that population means between CT and MRI are the same. These results would indicate a favorability to using MRI as a replacement imaging modality to CT; however, looking at the confidence intervals created for each comparison, it is noticeable as to why there were such favorable adjusted p-values. As seen in **Figure 5**, the 95% confidence intervals for the mean differences are drawn and show intersection with the line representing zero mean difference (indicating no significant difference). With the variance increasing over time though, it led to an increasing confidence interval as well. With the wide confidence interval, it is more evident why the adjusted p-values showed little significance between the two imaging modalities' means.

Furthermore, there is concern in the characteristics of the data set compared to CT. **Table 4** should serve as a one-to-one comparison between CT and MRI data, since each subject was imaged using both modalities within 24 hours of one another. Given that CT is the standard for lung imaging, the CT data serves as the standard to compare the MRI to. Looking specifically at the 8 week time point, it shows subject 180 had severe RIPF whereas MRI was unable to capture this severity (**Fig. 6**). The segmentation on the CT image led to a fibrosis fraction (V_F/V_T) approximately double the fraction calculated from the MR segmentation: 0.4618 and 0.2338 respectively. One would hope that MRI would be able to capture such severity if it were to be used to diagnose or track RIPF.

Conclusions and Future Directions

Due to the MRI's inability to adequately capture the severity of RIPF as well as CT, it is not recommended as an alternative imaging modality for RIPF. Although it was previously conjectured that the radiation sparing attribute of MRI would greatly benefit the RIPF model, the dose spared to the subjects is minimal enough for it to be considered nominal. For MRI to be of any benefit, its contrast and resolution would need to be improved.

A hypothesized means of contrast enhancement was to use F-19 imaging for the MRI. MRI lung studies have previously used this method.[47,48] Since Isoflurane was used as the anesthetic to minimize motion during scanning, we conjectured that using F-19 imaging and a custom-made coil could detect absorption concentrations of the fluorine in isoflurane. However, this project required more engineering and time than expected, so it was not pursued further.

Resolution for the MR images could also be improved by utilizing the UTE 3D scan instead of the axially sliced UTE scan used in this study. Segmentations for MR images proved more difficult due to the poor resolution in the dorsal and sagittal planes. The auto-segmentation feature in ITK-SNAP struggled to expand segmentation bubbles between slices, which left several areas needing to be manually segmented.

MRI has shown great promise in aiding researchers to discover greater details of models that may have gone unnoticed. Because of MRI's greater tissue contrast, features of soft tissue that go missed in CT images can be observed. With several adjustments made to the UTE scan presented in this paper, RIPF could be modeled using MRI which could provide new details to the RIPF model that were previously unknown.

CHAPTER 4: MURINE RADIATION-INDUCED STOMACH PATHOLOGY FROM WHOLE THORACIC IRRADIATION

Daniel R. McIlrath, MS[1], and Carlos J. Perez-Torres, PhD[1,2*].
[1]*School of Health Sciences, Purdue University, West Lafayette, Indiana, US*
[2]*Purdue University Center for Cancer Research, Purdue University, West Lafayette, Indiana, US*

[1]Address for correspondence: School of Health Sciences, Purdue University, 550 Stadium Mall Drive, Hampton Hall 1263A, West Lafayette, IN 47907, USA; cperezto@purdue.edu

Abstract

Background: Mouse models of radiation-induced lung injury are commonly produced to find novel treatments for the condition. While attempting to irridiate mouse lungs for purposes of creating such a model, noticable declines in health were observed at much earlier time points than recorded for lung pathology. These effects were attributed to off-target effects from imprecise radiation delivery.

Methods: Verification of radiation localization was performed through film dosimetry of the irradiated thorax. Male C57Bl/6 mice were irradiated with a single dose of 20 Gy to the whole thoracic area delivered by an X-Rad cabient irradiator. CT was performed with respitory gating at 2 to 4 week timepoints to which identified abnormal pathology *in vivo*. Confirmation of CT findings was performed via histology on the stomachs using hematoxylin and eosin staining.

Results: On the CT images, we observed a large, spherecal volume of hypointense signal, caudal to the lungs as easrly as 4 weeks post irradiation. This correlated with a distended stomach caused by constipation and gas build-up within the stomach. Statistical anlysis showed 81% of mice (n=105) died prematurely after irradiation before the desired development of pulmonary fibrosis. Mice sacrificed and disected showed unpassed bolus as contents of the stomach, and histology showed cell metaplasia of the stomach walls.

Conclusion: Imprecise radiation dose delivery to the lungs lead to unexpected pathology of the stomach. Future studies need to consider careful placement of shields or any beam contouring devices to ensure protection of the stomach given its higher radiosensitivity in contrast to the lungs.

Keywords: Animal models, radiation biology, computed tomography, thoracic irradiation

Introduction

Thoracic irradiation treatments are among the most common in external beam cancer therapies largely due to the high incidence of breast and lung cancer – the two most prevalent cancers in the world. Lung cancer is the most frequently diagnosed cancer with 1.6 million new cases each year [2] and breast cancer is the second most frequently diagnosed cancer with 1.1 million new cases each year [41,42]. Proving to be an effective treatment, radiation therapy ideally destroys all of the cancer's tumor cells while maintaining healthy cells' integrity. However, the ideals prove to be far from realistic with 35% of thoracic irradiation patients at risk to develop lung injury [7–9]. The risk of radiation-induced lung injury, which has limited treatment options, limits the amount of radiation that can be safely delivered to the tumor. Research into the mechanisms and potential therapeutics are usually performed in mouse models that replicate the clinical disease [11,43].

To create such a model, accurately contouring the beam becomes vital due to the small nature of the mouse's organs and the nearby relative radiosensitivity of neighboring organs – including the liver and the stomach [49]. Clinically, this is possible through a combination of multi-leaf collimators and on-board imaging to contour the radiation beam to the desired treatment field with great efficacy. Pre-clinical studies rarely have access to such sophisticated devices and rely on simple radiation machines, such as cabinet irradiators, to deliver the experimental dose. These crude devices, in comparison to LINACs, lack the ability to contour beams as accurately, and therefore, require subjects be shielded to protect areas not being researched [43].

Improper shielding can lead to unexpected off-target effects, particularly of tissues that are radiosensitive. These off-target effects could potentially present a confound that may obfuscate the intended results particularly if the measurement outcome is not specific enough. One such outcome is the use of mortality to evaluate rodent models of radiation induced lung injury. Here we report on unintended stomach toxicity in a model of radiation-induced lung injury. After our initial dose

deliveries, a large number of mice died less than a month after irradiation. These premature deaths greatly inhibited our study of the lungs, but the cause of the deaths were uncertain. CT scans revealed distended stomachs of several subjects which lead to the conclusion that our shielding was not sufficiently protecting the area caudal to the thorax, and the stomach was receiving harmful doses of radiation. Our shielding needed to be altered to ensure the protection of any radiosenstive organs from sustaining harmful doses.

Methods

All animal experiments were approved by the Purdue Animal Care and Use Committee.

Mouse Characteristics

Mice used to develop our model was determined based on previous literature[11]. Male C57Bl/6 mice were used due to their reported radioresistance compared to female mice and their historically published pro-RIPF characteristics. Radiosensitivity was of concerned because previous trials preformed lead to premature death leading to the decision to use mice that were more likely to survive irradiation. Mice were irradiated at 8 weeks-old and weight was not tracked.

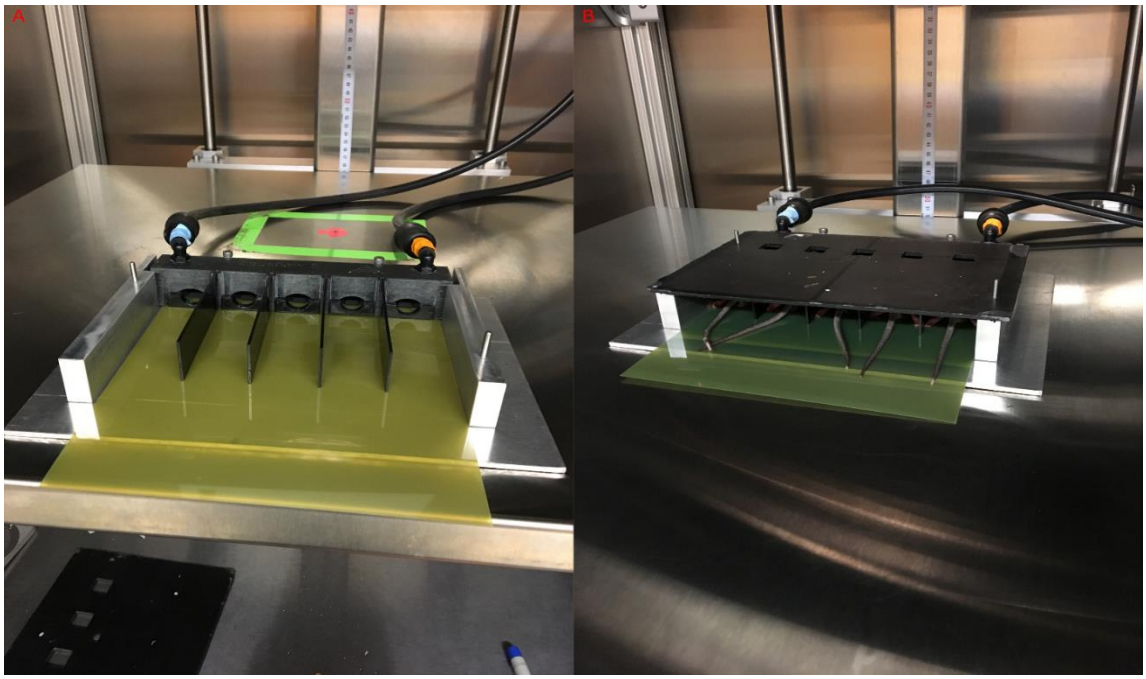

Figure 22: Irradiation setup with **[A]** a 5-chamber platform and attached to a sedative delivery system with a piece of Gafchromic EBT 3 film slid in between the floor of the platform and the mice. **[B]** Mice placed in chambers with lead shielding placed above to contour the x-ray beam to irradiate the thorax of each mouse to deliver 20 Gy to only the lungs.

Mice were housed in a facility located on Purdue University's campus and maintained by Purdue University's animal care staff. Mice were checked daily by staff and weekly by researcher during imaging dates. Mice that developed severe wounds due to erythema, bullying, or other causes were checked every other day. Euthanasia would be deemed necessary by animal care staff when wounds, after treatment, progressed or remained severe.

Irradiations

Based on previous studies[11], mice were irradiated with a single fraction dose of 20 Gy to the whole thoracic region with a 320 kV cabinet irradiator (X-Rad 320, Precision X Ray, North Branford, CT). Mice were sedated with Isoflurane in an induction chamber and then kept sedated through a custom made anesthesia manifold (**Figure 16A**). Mice were sedated in groups of five and placed on the platform in the prone position with Gafchromic EBT 3 film (Ashland Advanced Materials, Bridgewater NJ) placed beneath for position validation. Lead shielding was then placed above the mice (**Figure 16B**) with a 15 mm x 15 mm aperture placed above the thorax of each

mouse. Later, because of the findings presented herein, a second shield was utilized with an 7.5 mm x 15 mm aperture reducing the height in half from the first shield. Each mouse was adjusted individually to optimize positioning for dose delivery. The cabinet irradiator was set to deliver a dose of 20 Gy with a dose rate of approximately 200 cGy/min and a tube setting of 320 kV. Source-to-skin distance was set to be 50 cm and a 0.1 mm Al beam flattening filter was used. Irradiations took approximately 10 minutes to deliver the desired dose given the dose rate. Afterwards, mice were allowed to recover from anesthesia in their cages under observation and returned to the mouse facility.

Film Analysis

Film irradiated during dose delivery was analyzed using an EPSON Perfection V600 photo scanner and the software program ImageJ. After scanning films, the corresponding files were opened with ImageJ where their RGB channels were separated into three individual images. The green channel offered the most contrast for Gafchromic EBT 3 film, so it was used to validate subject positioning during irradiation [44].

Assessment of pathology

Mice were imaged using a pre-clinical Perkin-Elmer Quantum Lab GX X-ray microCT in 2-4 week time points. Mice were anesthetized using isoflurane in order to slow down breathing and make respiratory gating possible and then placed within the bore of the microCT. Images were acquired using respiratory gating and with a 72 mm FOV and then reconstructed with a 36 mm FOV which will incur a dose to the subject of approximately 162 mGy. Mice that showed distended stomachs were euthanized using Isoflurane and had their stomachs removed and placed in 4% paraformaldehyde. Stomachs were then sliced along its longitudinal axis and placed in 70% ethanol and then embedded in paraffin to generate 4 micron slices. Slices were stained with hematoxylin and eosin and visualized with an Evos-XL light microscope.

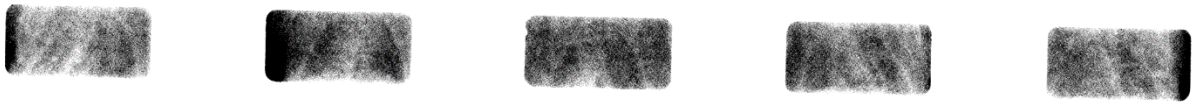

Figure 23: Film of 5 mice's positions relative to the 2.5 $mm\ x\ 5\ mm$ aperture in the lead shielding. It is evident from these films that positioning of the mice lungs are well contoured to adequately irradiate the entirety of the lung.

Results

Evidence of irradiation beyond the lungs.

The original goal of our study was to evaluate a mouse model of radiation-induced lung injury. As a quality control measure, we utilized radiographic film to image the portions of the mouse that received irradiation. It was noticed that some of the mice were misaligned since the aperture was larger than the size of the lungs, and large portions of liver and stomach were receiving the same dose as the lungs (**Figure 17**). Base on this observation a new lead shield was generated which reduced the size of the aperture by half. By changing the size of the aperture within the lead shielding we reduced the amount of non-lung tissue that was irradiated as evidenced by **Figure 17**. Even so, as the position of the mice were not perfectly consistent between cohorts there might still have been some variation with regards to the localization of the irradiation field.

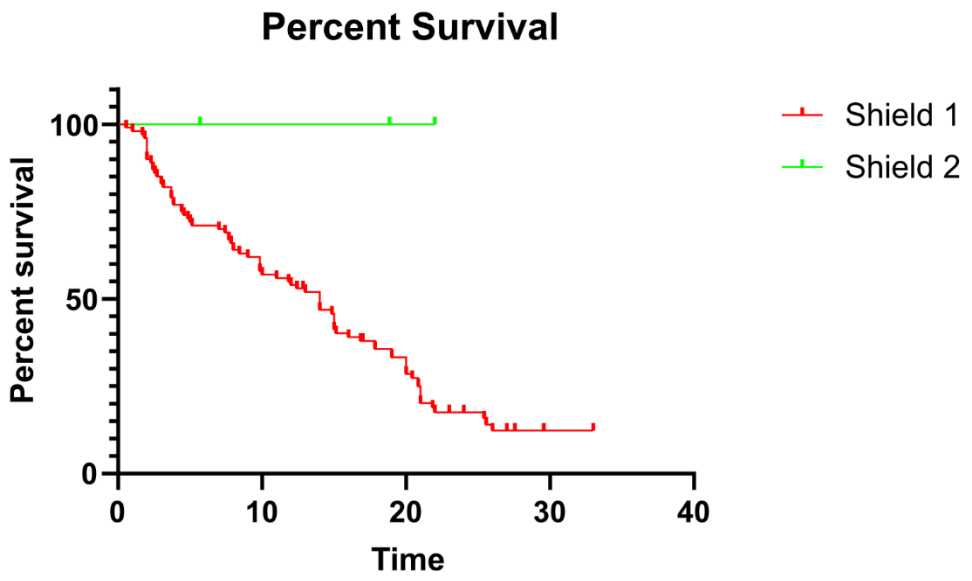

Figure 24: Survival of mice irradiated with shield 1 and 2. Mice survived significantly longer when shield 2 was used in place of shield 1 to irradiate the mice. This led to the conclusion that by minimizing the aperture size, positioning was made easier and a tighter exposure field to the lungs was more possible.

Off-target effects lead to premature mouse death

The major consequence of the larger irradiation field was mice died only a few weeks after radiation (**Figure 18**) whereas death due to fibrosis should occur at ~24 weeks post irradiation at our given radiation dose [11]. After changing to the shield with the smaller aperture (shield 2) the premature deaths were minimized though given the inconsistencies previously noted (**Figure 17**) there is still a risk for off-target effects. These numbers indicated an improvement to our experimental design that allows a greater number of subjects to survive to exhibit the desired pathology.

Stomach Pathology can be identified on CT and verified on histology.

The premature deaths in our study are at least partially due to unintended stomach pathology. On CT examination the normal stomach appeared as a minimal hyperdense area with a few gas pockets visualized as hypodense spots (**Figure 19A**). For a mouse that died prematurely, the stomach is observed as a large hypodense area just caudal to the left lung (**Figure 19B**). This

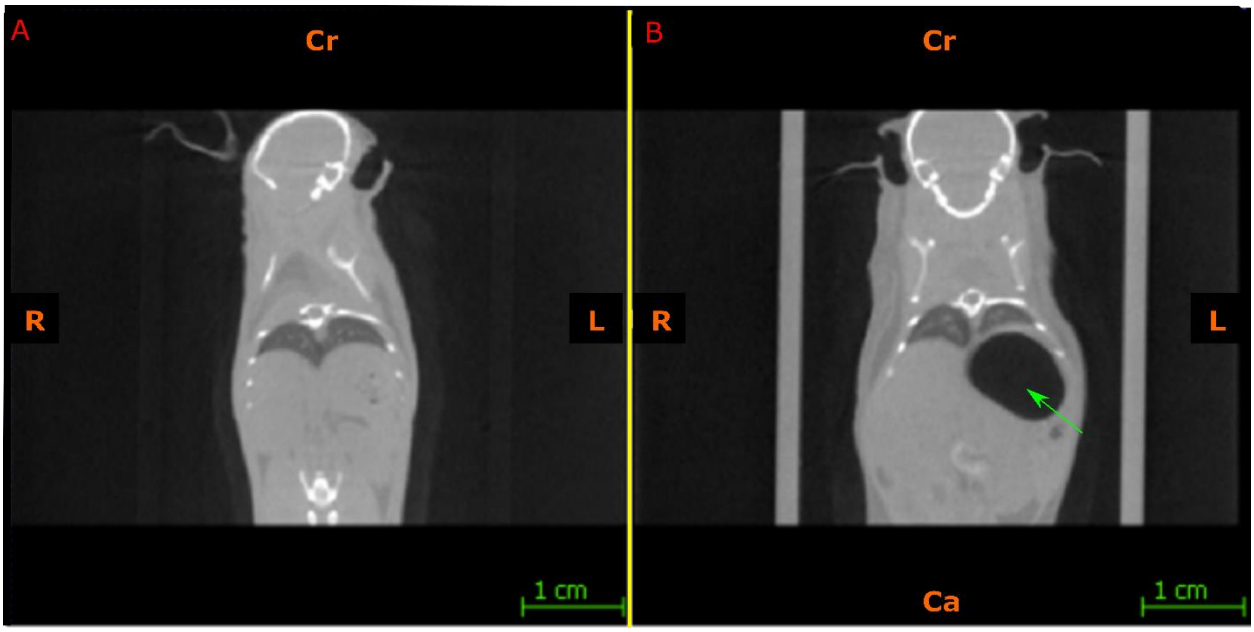

Figure 25: CT image of thorax **[A]** pre-irradiation and **[B]** 10 weeks post-irradiation. The mouse's stomach has a large area of hypodensity caudal to the left lung (green arrow). This area coincides with the stomach and the abnormal size of this area implies the stomach is distended. Although specific dosimetry would need to be done to determine the exact dose received by the stomach, the dose that we delivered led to high enough doses being absorbed by the stomach to cause early injury that jeopardized the efficacy of the study.

CT hypodensity could be observed as early as 4 weeks post irradiation which is consistent with the timing of premature death. That the stomach is distended and hypodense on CT suggests a large buildup of gas, likely due to the inability to break down food.

Histology shows major gaps in the middle section of the fundic region of the mouse's stomach (**Figure 20**). The basal and superficial layers appear to show little alteration; however, there is evident metaplasia that appears to extend from the superficial layers through the middle to basal layers. The most radiosensitive cells of the fundic region are the eosinophilic parietal cells of the middle layer which secrete acid for digestion, and the next most sensitive would be the mucosa-secreting cells of the foveolar column of the basal layer [50,51]. The desquamation of the mucosa most likely lead to ulcerations (**Figure 20B**).

Discussion

Preclinical rodent models of radiation –induced pathology are commonly used in the development of novel therapies for these conditions. Generation of these models requires that radiation be delivered precisely as off-targets effects can obfuscate the findings. In our data, off-

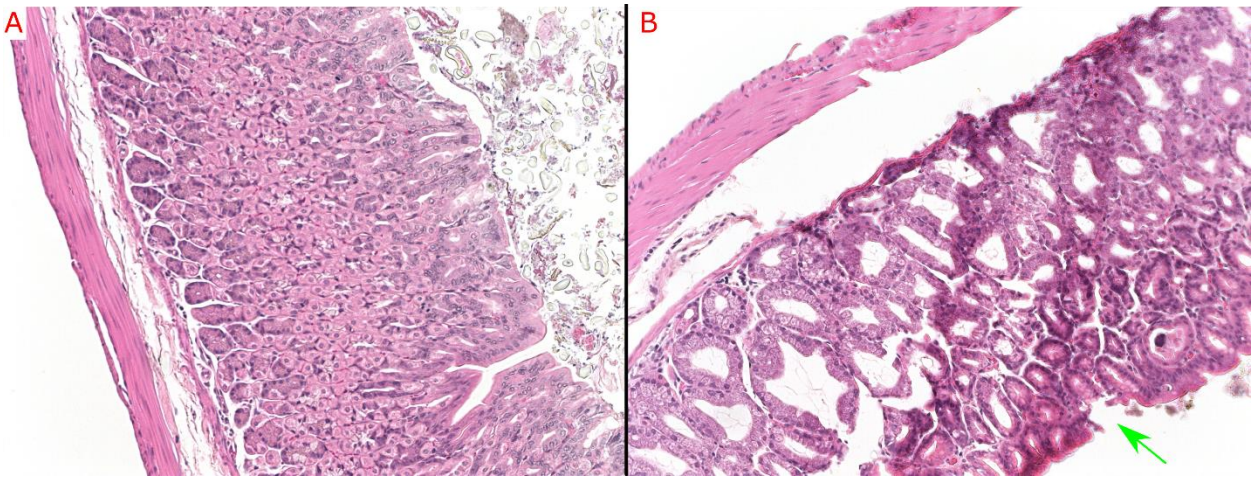

Figure 26: Histology slides with Hematoxylin and Eosin staining at 20x multiplication. **[A]** A control mouse's glandular stomach showing the three main layers: basal layer, middle layer, and superficial layer. **[B]** Similar stomach slice location for 15 week post-irradiation mouse. The middle layer's parietal cells, which secretes acidic fluids, appears necrotic and poorly structured. An apparent ulcer appears in the basal layer of the stomach wall (green arrow). This indicates the desquamation of mucosa that protected the stomach wall from acid erosion and injury to the mucosa-secreting cells of the foveolar column.

target radiation delivery lead to premature death. Stomach distention became salient on CT images of any effected mice and indicated improper radiation delivery. This could be further verified by the films produced during irradiation. When the radiation field size was changed by adjusting the aperture size on the shielding, significant changes in survival were observed. Histology provided even more evidence of the injury to the stomach that aligns with previous studies on stomach radiation toxicity [49].

Due to the salient stomach distention observed on CT images, the stomach was the focus of this tangential observation during lung modeling. Liver was considered as a possible organ at risk but quickly dismissed due to its radioresistance compared to the stomach and lack of pathology observed on the CT images. The gastro-intestinal tract and other distal structures to the lung were not considered in our study since the misalignment of the mice was minimal enough to not expose extremely caudal features and our misalignment was always exposing the abdomen, so no organs cranial to the thorax were considered.

During external beam treatments, the human stomach often receives residual dose from targeted tumors in the upper gastrointestinal tract or inferior lung. If the stomach receives around 15 Gy in a single fraction, late-effects begin to be of concern despite the volume of the stomach irradiated.[52] Patients that have received around 67 Gy total through fractionation have reported ulcers occurring post-irradiation [50]. In a three-fraction stereotactic body radiation treatment , dose-

volumes are required to be minimized to 22.5 Gy to 5 cc of stomach [52]. In rodents, doses above 14 Gy, delivered in a single fraction to the whole stomach, showed significant risk in the development of acute- and late-effects and eventually mortality [53]. Since doses for pre-clinical lung studies are close to this threshold, it is extremely important to thoroughly protect the stomach during these studies.

Conclusion

Though we were able to confirm the presence of stomach pathology in a few of our mice that died prematurely, there were also some mice where necropsies could not be performed. Some premature deaths are left out of this analysis since their cause of death was known – overdose of anesthetic during imaging – although this number was small (n=8). The premature deaths, presumably caused by stomach pathology, were a major challenge to our primary study focused on radiation-induced pulmonary pathology. This challenge was further exacerbated in the case of the mice for whom necropsy was not feasible. Without necropsy it was not possible to ascertain whether death was due to lung pathology or unintended pathology. This also further demonstrates the limits of using survival as a metric for specific form of radiation-induced pathology. For this reason, it is important to create adequate protection and develop a mold that provides more precise subject placement in future lung studies to prevent a loss of potential data and time.

Unfortunately, since this was an unplanned pathology that occurred during research for a completely different radiation injury, there is a lot of uncertainty in the results due to the lack of a well-defined experimental design. Many secondary factors such as diet were not controlled and need to be. Further study could be done by minimizing explanatory variables and statistically analyzing their significance on the response variable – stomach distention. Also, a more quantifiable analysis could be performed if stomach volume could be recorded along with the explanatory variables over time. From this data, a better model could be formed to further benefit anyone performing a pre-clinical study with a similar methodology to this study.

For those performing similar studies, it is highly recommended to create shielding with dimensions that tightly contour the borders of the thorax (i.e. the lungs). We continued to use the 7.5 mm x 15 mm shield aperture since it guaranteed to expose a large portion of the lung without exposing areas beyond the thorax. If possible, a mold would be beneficial to immobilize the mice

and minimize uncertainty in positioning; however, time and resources prevented us from obtaining such a mold.

List of abbreviations
CT – Computed tomography

Declarations
Ethics approval and consent to participate
All animal experiments were approved by the Purdue Animal Care and Use Committee.

Consent for publication
"Not applicable"

Availability of data and materials
"The datasets used and/or analyzed during the current study are available from the corresponding author on reasonable request."

Competing interests
The authors have no conflicts of interest to disclose.

Funding
There are no funding sources to report for this study.

Authors' contributions
DRM designed and performed the experiments, analyzed the data, and wrote the manuscript. CJPT oversaw experiments and wrote the manuscript.

Acknowledgments
The authors acknowledge the assistance of the Purdue University Histology Laboratory, a core facility of the NIH-funded Indiana Clinical and Translational Science Institute, for the processing of the tissue sections and H&E staining. We also wish to thank Dr. Chang-Deng Hu for providing access to the X-Rad 320.

CHAPTER 5: FUTURE DIRECTIONS AND CONCLUSION

Key Findings

From our research, it was noticeable how effective the CT imaging and segmentations were at quantifying RIPF volumes. This method of analysis led to a wealth of information that provided information on RIPF's development and exposed its discrepancy in severity within later time points. From our model, we could tell that around 10-12 weeks was when RIPF had developed enough to be radiologically detected; however, significant differences existed at the later time points suggesting the time at which RIPF's onset occurs was not consistent.

The resulting effect of this severity discrepancy was an increase in variance among time points. This variability also inhibited our statistical analysis by creating a larger pooled standard deviation that was used for the ANOVA. This large variability cast doubt on how significantly different the population means were from the baseline and if they were different at all. Regardless of the variability, significant increases in RIPF were seen and this analysis will provide a model that can be used in the future. Also, despite expectations, tidal lung volumes provided no statistically significant characteristics between time points.

We additionally found it feasible for MRI to replace CT to image RIPF as a means to create a more sensitive model and exclude any possible mistakes in labeling tumor recurrence or infections as RIPF. However, we also discovered the radiation spared by not using CT was not significant enough to eliminate any desire to sacrifice CT's high spatial resolution for MRI's poor resolution. Although our study on MRI's feasibility to image RIPF raised concerns, future actions can be taken to improve upon our methodology and produce higher contrast and resolution images for more accurate volume segmentations of RIPF.

We also inadvertently saw the necessity of shielding organs outside of the thorax to prevent premature mortalities. Although intuitive, it was an easy oversight to create a shield for the mice irradiations that had too large of apertures to sufficiently protect the organs adjacent to the thorax.

Impact

Radiation models are of great interest currently due to fears of impending nuclear warfare and disasters.[38] With sufficient models, disease pathogenesis and occurrence can be thoroughly

understood to aid in responses to such catastrophes. Beyond these global impacts, cancer survivors frequently must deal with the sequelae of their radiation therapy. Even if the treatment successfully heals a patient's primary cancer, they have to make routine appointments post-treatment to be checked for RIPP and RIPF, where they have to fear possibly developing a secondary, fatal illness in RIPF. Unfortunately, few actions can be taken post-therapy to inhibit or prevent RIPF which creates further hardship in the life of a cancer survivor if he or she were to develop RIPF. Studies on the molecular mechanisms that lead to RIPF are the current hope to provide answers to how this pathology can be stopped, but there is still a lot to be uncovered. These studies focus on various inflammatory cytokines and immune response cells to create biomarkers that lead to RIPF. If these biomarkers indicate RIPF, regulating or inhibiting their responses may lead to an RIPF prevention treatments. However, studies currently evaluate these biomarkers through blood draws and analysis,[54] so an *in situ* analysis would greatly benefit a model by providing *in vivo* data of biomarker levels for comparison to treatment responses.

For any study though, a standard, control model has to be developed which takes time. The intention of this research was to build upon the work of previous studies to form an improved, more clinically relevant control model of RIPF. With previous studies focusing on mortality rates, previous models are unable to provide intermediate analysis for pre-clinical treatment studies to determine treatments' effectiveness, prognosis, or time to onset. With our RIPF murine model, researchers will be able to assess treatments by comparing their results with ours. Our model will also provide intermediate analysis of RIPF development, so researchers can create timelines of treatments' effectiveness and recognize any temporal significant differences as well.

Future Directions

Model Issues

The greatest weakness of our CT model is its poor sample sizes along time points, minimal validation of segmented RIPF volumes, and the clinical irrelevance of WTI.

Future studies would need to adjust our method of mouse irradiation to better prevent secondary pathologies and also keep a more consistent subject imaging schedule to provide greater and equal sample sizes at every time point. Given the depleted sample sizes at later time points and despite our adjustment to the shielding, mice were still dying prematurely. The reason for these

premature deaths would most aptly be attributed to the mice's development of erythema. The cabinet irradiator used to deliver our doses was of lower energies, so significant dose was absorbed by the skin. Mice would scratch incessantly at the erythema – to the point of forming open wounds. This would force the euthanization of a subject and, thus, its removal from the study's future time points. If a higher energy irradiator or alternative method could be used to spare the skin, it would provide greater chances of subjects surviving to later time points. Unequal sample sizes at time points is best attributed to poor scheduling and subject overload during data collection.

Moreover, autopsy and histology need better consistency to provide proper validation of pathology. Mice lungs prove difficult to dissect, and a lung mold that would allow for more consistent dissections would aid in a future validation study. In the analysis of our RIPF model, we fail to fully validate the presence of hyperintensity of CT images as RIPF. Our intentions were for our histology to be our source of validation; however, we only used the histology to validate the presence of RIPF and not necessarily specifically validate what areas on CT images spatially correspond to respective histology images. In order to achieve this, a 1-to-1 mapping would be necessary between the hyperdense areas on a subject's final CT image and the blue, collagen deposits on the Mason's trichrome stained histology slide.

WTI affects results due to increased sensitivity due to the lung's high dose-volume sensitivity. Altering radiation delivery would provide a more clinically-relevant model and eliminate the lung's dose-volume sensitivity from impacting results. Two ways of doing this would include, but is not limited to, partial lung irradiations and fractionated dose deliveries. Additionally, our model is focused on a specific dose delivery instead of a grading dose response. Applying our methodology to gradient delivered doses will aid in developing timelines of RIPF onset and dose-related prognoses.

Next Steps

Molecular Mechanisms

The primary goal of this research is ultimately to aid in the discovery of treatment that will inhibit or prevent the development of RIPF post-treatment by modeling standard RIPF development in mice as a control group. As previously mentioned, great hope has been placed in finding a biological pathway that can be manipulated to downregulate or block pro-fibrotic and

pro-inflammatory responses. Several possible pathways are known but tracking these biomarkers have yet to be done *in situ*. This opens up the possibility to track protein levels and presence through use of a tracer attached to a radioactive agent. PET/SPECT imaging opens doors for analyzing biomarkers such TNF-α and TGF-β that have been shown to play large roles in RIPF pathogenesis.[7,15,55] A previous study has shown a similar method by using Tc^{99m}-macroaggregated albumin to detect altered pulmonary perfusion and Tc^{99m}-labeled Duramycin which binds to apoptotic cells to track functional changes through these biomarkers and indicate possible RIPP development.[55] Another study shows that Transmembrane TNF-α is a ligand that is able to bind to TNF-α, so if the ligand could be labeled with a tracer, either Tc^{99m} for SPECT or FDG for PET, then a study could find *in vivo* TNF- α levels and correlate them to RIPF onset.[56] Similar studies could be performed for the myriad of speculated pro-fibrotic cytokines.[40,57–59]

In all these cases, an experimental drug would need to be delivered to test its efficacy on any response variable – this could include any of the cytokine expressions or overall RIPF radiological volume expression. Experimental drugs can be delivered in three ways: prevention, mitigation, and treatment. Prevention drugs are delivered prior or concurrent to radiation delivery, mitigation drugs are delivered after exposure but before disease onset, and treatment drugs are delivered post disease onset. In the first two cases, the drug has the same aim – to prevent or inhibit disease onset. However, in the later case, treatment drugs have the goal to reverse pathology. As previously stated, RIPF is irreversible, so treatment drugs would prove to be ineffective and palliative at best. Therefore, knowing time to onset is extremely important to demarcate the latest time for mitigating drug intervention. Previous models fail in providing this pertinent information to pre-clinical trials.

Through adapting our dose delivery to only a part of the mouse's lung, trials will have a model that provides onset times of RIPF while eliminating the dose-volume response. This model will be the most clinically relevant and provide studies the ability to asses optimal drug delivery times post-exposure. Studies could use our data and vary drug delivery times post-exposure to see if the delivery time affects specific cytokine levels or RIPF volumes positively or negatively. Optimal delivery time would be the one that ultimately minimizes RIPF volumes significantly weeks post-exposure or prevents any consolidation development and hyperdense volume increase.

^{19}F MR Imaging

Using MRI to model RIPF is still in its infancy through our study and only its feasibility to do so has been shown. Many methods have been created to enhance the contrast of MR lung images such as fluorine-19 imaging. By changing the coil and adjusting the MRI's settings to detect resonance frequencies of F-19 (γ~40.05 MHz/T) instead of water/protons (γ~42.58 MHz/T), a fluorinated contrast agent can be administered to detect its diffusion throughout the subject.[47] Such contrast enhancement would aid in producing greater signals from within the lung to better study pathology. An attempt to achieve this was made by crafting an in-house dual-tuned coil to detect F-19 and H-1 frequencies simultaneously.[48] However, the coil proved too difficult to build, so a single-tuned F-19 coil was built instead. Although some early results showed promise, with signal being acquired from a large vial of isoflurane, future attempts to acquire signal from smaller volumes of isoflurane were unsuccessful. If engineered correctly, F-19 imaging could lead to greatly enhanced MR imaging of the lungs and advance the model further.

Another direction that could be taken for future MRI RIPF model studies is improving the contrast and resolution of our MRI scan sequence. Improving the resolution of the scan could easily be done by utilizing the UTE 3D instead of our sliced UTE. This would allow the auto-segmentations to more accurately cover hypointense areas.

Conclusion

Currently, RIPF mouse models rely too heavily on MST and percent survival rates as determining characteristics for dose response and treatment intervention. Although this endpoint is of concern, there are still clinically relevant, intermediate time points of importance to understand RIPF's development. Essentially, treatments should be analyzed beyond simply time to mortality. Our models provide quantified RIPF tracked over weeks so individual subjects' or experimental groups' RIPF volumes can be compared to our results to determine increased or decreased RIPF onset or severity. These comparisons provide greater characterization of an experimental group and the effectiveness of the tested variable. By providing our methodology to develop a base model, future pre-clinical studies can expedite their research by utilizing our model or developing their own using our methods.

Pre-clinical studies are the origin of all current clinical treatments. It is necessary to study any theoretical and experimental using animal models before advancing to human trials. By studying and advancing current RIPF mouse models beyond the mortality rate, information is more readily known of how to create nuclear disaster and post-RT models using mice and tracking lung sequelae. Our model takes the next step in providing understanding of RILD's late phase and quantifying the pathology. Our model opens the door for more advanced imaging techniques in MRI to provide better sensitivity in our RIPF model and spare healthy lung tissue unnecessary dose. We showed how easy it was to allow a simple oversight in dose delivery to majorly affect the entire study and how to rectify our mistake, so future researchers do not have to waste valuable resources and time in their study. With these models and our proven methodology, another step is taken to understand and test experimental treatments for cancer patient survivors and radiation disaster victims, so they will not be afflicted by a future death sentence of RIPF after already escaping one.

REFERENCES

1. Grantzau, T. Risk of second primary lung cancer in women after radiotherapy for breast cancer - ScienceDirect. https://www.sciencedirect.com/science/article/pii/S0167814014001844.
2. McErlean, A. & Ginsberg, M. S. Epidemiology of Lung Cancer. *Semin. Roentgenol.* **46**, 173–177 (2011).
3. Li, C. I.-F. & Li, C. *Breast Cancer Epidemiology*. (Springer, 2009).
4. Hanania, A. N., Mainwaring, W., Ghebre, Y. T., Hanania, N. A. & Ludwig, M. Radiation-Induced Lung Injury: Assessment and Management. *Chest* (2019) doi:10.1016/j.chest.2019.03.033.
5. Ghaye, B., Wanet, M. & El Hajjam, M. Imaging after radiation therapy of thoracic tumors. *Diagn. Interv. Imaging* **97**, 1037–1052 (2016).
6. Marks, L. B. *et al.* Radiation-induced pulmonary injury: symptomatic versus subclinical endpoints. 8.
7. Chen, Z., Wu, Z. & Ning, W. Advances in Molecular Mechanisms and Treatment of Radiation-Induced Pulmonary Fibrosis. *Transl. Oncol.* **12**, 162–169 (2019).
8. Vågane, R., Bruland, Ø. S., Fosså, S. D. & Olsen, D. R. Radiological and functional assessment of radiation-induced pulmonary damage following breast irradiation. *Acta Oncol.* **47**, 248–254 (2008).
9. Lierova, A. *et al.* Cytokines and radiation-induced pulmonary injuries. *J. Radiat. Res. (Tokyo)* **59**, 709–753 (2018).
10. Rajan Radha, R. & Chandrasekharan, G. Pulmonary injury associated with radiation therapy – Assessment, complications and therapeutic targets. *Biomed. Pharmacother.* **89**, 1092–1104 (2017).
11. Dabjan, M. B. *et al.* A survey of changing trends in modelling radiation lung injury in mice: bringing out the good, the bad, and the uncertain. *Lab. Invest.* **96**, 936 (2016).
12. Park, K. J., Chung, J. Y., Chun, M. S. & Suh, J. H. Radiation-induced Lung Disease and the Impact of Radiation Methods on Imaging Features. *RadioGraphics* **20**, 83–98 (2000).
13. Larici, A. R. *et al.* Lung Abnormalities at Multimodality Imaging after Radiation Therapy for Non–Small Cell Lung Cancer. *RadioGraphics* **31**, 771–789 (2011).

14. Choi, Y. W. *et al.* Effects of Radiation Therapy on the Lung: Radiologic Appearances and Differential Diagnosis. *RadioGraphics* **24**, 985–997 (2004).

15. Ding, N.-H., Li, J. & Sun, L.-Q. Molecular Mechanisms and Treatment of Radiation-Induced Lung Fibrosis. *Curr. Drug Targets* **14**, 1347–1356 (2013).

16. Hübner, R.-H. *et al.* Standardized quantification of pulmonary fibrosis in histological samples. *BioTechniques* **44**, 507–517 (2008).

17. Järvenpää, R. *et al.* Radiological pulmonary findings after breast cancer irradiation: A prospective study. *Acta Oncol.* **45**, 16–22 (2006).

18. *Magnetic resonance imaging: physical principles and sequence design*. (Wiley-Liss, 1999).

19. Holmes, J. E. & Bydder, G. M. MR imaging with ultrashort TE (UTE) pulse sequences: Basic principles. *Radiography* **11**, 163–174 (2005).

20. Kern, A. L. & Vogel-Claussen, J. Hyperpolarized gas MRI in pulmonology. *Br. J. Radiol.* **91**, (2018).

21. Qing, K. *et al.* Regional mapping of gas uptake by blood and tissue in the human lung using hyperpolarized xenon-129 MRI. *J. Magn. Reson. Imaging* **39**, 346–359 (2014).

22. Santyr, G. *et al.* Anatomical, functional and metabolic imaging of radiation-induced lung injury using hyperpolarized MRI. *NMR Biomed.* **27**, 1515–1524 (2014).

23. Flors, L. *et al.* New insights into lung diseases using hyperpolarized gas MRI. *Radiol. Engl. Ed.* **57**, 303–313 (2015).

24. Benveniste, M. F. K. *et al.* New era of radiotherapy: An update in radiation-induced lung disease. *Clin. Radiol.* **68**, e275–e290 (2013).

25. Aoki, T. *et al.* Evaluation of Lung Injury after Three-dimensional Conformal Stereotactic Radiation Therapy for Solitary Lung Tumors: CT Appearance. *Radiology* **230**, 101–108 (2004).

26. Davis, S. D., Yankelevitz, D. F. & Henschke, C. I. Radiation effects on the lung: clinical features, pathology, and imaging findings. *Am. J. Roentgenol.* **159**, 1157–1164 (1992).

27. Dileto, C. L. & Travis, E. L. Fibroblast radiosensitivity in vitro and lung fibrosis in vivo: comparison between a fibrosis-prone and fibrosis-resistant mouse strain. *Radiat. Res.* **146**, 61–67 (1996).

28. Sharplin, J. & Franko, A. J. A quantitative histological study of strain-dependent differences in the effects of irradiation on mouse lung during the intermediate and late phases. *Radiat. Res.* **119**, 15–31 (1989).
29. Eichinger, M. *et al.* Morphologic and functional scoring of cystic fibrosis lung disease using MRI. *Eur. J. Radiol.* **81**, 1321–1329 (2012).
30. Treuting, P. M., Dintzis, S. M. & Montine, K. S. Comparative Anatomy and Histology - 1st Edition. https://www.elsevier.com/books/comparative-anatomy-and-histology/treuting/978-0-12-381361-9.
31. Beach, T. A., Groves, A. M., Williams, J. P. & Finkelstein, J. N. Modeling radiation-induced lung injury: lessons learned from whole thorax irradiation. *Int. J. Radiat. Biol.* **0**, 1–16 (2018).
32. Down, J. D. & Steel, G. G. The Expression of Early and Late Damage after Thoracic Irradiation: A Comparison between CBA and C57Bl Mice. *Radiat. Res.* **96**, 603–610 (1983).
33. Jackson, I. L., Vujaskovic, Z. & Down, J. D. Revisiting Strain-Related Differences in Radiation Sensitivity of the Mouse Lung: Recognizing and Avoiding the Confounding Effects of Pleural Effusions. *Radiat. Res.* **173**, 10–20 (2010).
34. Travis, E. L. *et al.* NRF2 deficiency reduces life span of mice administered thoracic irradiation. *Free Radic. Biol. Med.* **51**, 1175–1183 (2011).
35. Jackson, I. L. *et al.* A Preclinical Rodent Model of Radiation-induced Lung Injury for Medical Countermeasure Screening in Accordance With the FDA Animal Rule: *Health Phys.* **103**, 463–473 (2012).
36. Fox, J. & Haston, C. K. CXC Receptor 1 and 2 and Neutrophil Elastase Inhibitors Alter Radiation-induced Lung Disease in the Mouse. *Int. J. Radiat. Oncol.* **85**, 215–222 (2013).
37. Jackson, I. L. *et al.* Characterization of the Dose Response Relationship for Lung Injury Following Acute Radiation Exposure in Three Well-established Murine Strains: Developing an Interspecies Bridge to Link Animal Models with Human Lung. *Health Phys.* **106**, 48–55 (2014).
38. Williams, J. P., Johnston, C. J. & Finkelstein, J. N. Treatment for Radiation-Induced Pulmonary Late Effects: Spoiled for Choice or Looking in the Wrong Direction? *Curr. Drug Targets* **11**, 1386–1394 (2010).
39. Cekan, E., Tribukait, B. & Vokal-Borek, H. Protective Effect of Selenium Against Ionizing Radiation-Induced Malformations in Mice. *Acta Radiol. Oncol.* **24**, 267–71 (1985).

40. Bury, T. *et al.* Value of FDG-PET in detecting residual or recurrent nonsmall cell lung cancer. *Eur. Respir. J.* **14**, 1376–1380 (1999).

41. *Breast Cancer Epidemiology*. (Springer, 2009).

42. Grantzau, T., Thomsen, M. S., Væth, M. & Overgaard, J. Risk of second primary lung cancer in women after radiotherapy for breast cancer. *Radiother. Oncol.* **111**, 366–373 (2014).

43. Medhora, M. *et al.* Whole-thorax irradiation induces hypoxic respiratory failure, pleural effusions and cardiac remodeling. *J. Radiat. Res. (Tokyo)* **56**, 248–260 (2015).

44. Borca, V. C. *et al.* Dosimetric characterization and use of GAFCHROMIC EBT3 film for IMRT dose verification. *J. Appl. Clin. Med. Phys.* **14**, 158–171 (2013).

45. Cella, L. *et al.* Modeling the risk of radiation-induced lung fibrosis: Irradiated heart tissue is as important as irradiated lung. *Radiother. Oncol.* **117**, 36–43 (2015).

46. Devore, J. L. *Probability and statistics for engineering and the sciences*. (Thomson/Brooks/Cole, 2008).

47. Fox, M. Fluorine-19 MRI Contrast Agents for Cell Tracking and Lung Imaging. *ResearchGate* https://www.researchgate.net/publication/299373438_Fluorine-19_MRI_Contrast_Agents_for_Cell_Tracking_and_Lung_Imaging doi:http://dx.doi.org/10.4137/MRI.S23559.

48. Hu, L. *et al.* A Generalized Strategy for Designing F-19/H-1 Dual-Frequency MRI Coil for Small Animal Imaging at 4.7 Tesla | Request PDF. *ResearchGate* https://www.researchgate.net/publication/51243640_A_Generalized_Strategy_for_Designing_F-19H-1_Dual-Frequency_MRI_Coil_for_Small_Animal_Imaging_at_47_Tesla doi:http://dx.doi.org/10.1002/jmri.22516.

49. Breiter, N., Trott, K.-R. & Sassy, T. Effect of X-irradiation on the stomach of the rat. *Int. J. Radiat. Oncol.* **17**, 779–784 (1989).

50. Oberdiac, P. & Mineur, L. Dose de tolérance à l'irradiation des tissus sains : l'estomac. *Cancer/Radiothérapie* **14**, 336–339 (2010).

51. *Comparative Anatomy and Histology: A Mouse, Rat, and Human Atlas*. (Academic Press, 2017).

52. Kavanagh, B. D. *et al.* Radiation Dose–Volume Effects in the Stomach and Small Bowel. *Int. J. Radiat. Oncol.* **76**, S101–S107 (2010).

53. Breiter, N., Sassy, T. & Trott, K.-R. The effect of dose fractionation on radiation injury in the rat stomach. *Radiother. Oncol.* **27**, 223–228 (1993).

54. Siva, S. *et al.* A Pattern of Early Radiation-Induced Inflammatory Cytokine Expression Is Associated with Lung Toxicity in Patients with Non-Small Cell Lung Cancer. *PLoS ONE* **9**, (2014).

55. Medhora, M. *et al.* Biomarkers for Radiation Pneumonitis Using Noninvasive Molecular Imaging. *J. Nucl. Med.* **57**, 1296–1301 (2016).

56. Horiuchi, T., Mitoma, H., Harashima, S., Tsukamoto, H. & Shimoda, T. Transmembrane TNF-α: structure, function and interaction with anti-TNF agents. *Rheumatol. Oxf. Engl.* **49**, 1215–1228 (2010).

57. Demirev, A. K., Kostadinova, I. D. & Gabrovski, I. R. 18F-FDG PET/CT in Patients with Parenchymal Changes Attributed to Radiation Pneumonitis. *Mol. Imaging Radionucl. Ther.* **27**, 107–112 (2018).

58. ZHANG, W. *et al.* Quantitative study of lung perfusion SPECT scanning and pulmonary function testing for early radiation-induced lung injury in patients with locally advanced non-small cell lung cancer. *Exp. Ther. Med.* **3**, 631–635 (2012).

59. Zhou, Y. *et al.* Noninvasive Imaging of Experimental Lung Fibrosis. *Am. J. Respir. Cell Mol. Biol.* **53**, 8–13 (2015).

VITA

Daniel R. McIlrath

EDUCATION

Ph.D. Medical Physics, *Purdue University (CAMPEP Accredited), West Lafayette, IN*…….. May 2020
M.S. Medical Physics, *Indiana University (CAMPEP Accredited), Bloomington, IN*…….. May 2016
M.A. Physics, *Ball State University, Muncie, IN*……... May 2015
B.S. Math/Physics Education, *Taylor University, Upland, IN*…..…….…..…. January 2012

MEDICAL PHYSICS EXPERIENCE **ABR Part 1 Passed (2018)**

Summer Practicum, *IU Health University Hospital, 2015*
Dr. Colleen DesRosiers, Associate Professor of Clinical Radiation Oncology, Indiana University

- Observed daily tasks and assisted with quality assurance checks
- Observed a cervical and prostate brachytherapy procedure
- Assisted with TG-51 protocol

Summer Practicum, *IU Health Bloomington Cancer Radiation Center, 2015*
Mr. Jeff Mumper, Medical Physicist, IU Health Bloomington Cancer Radiation Center

- Observed and participated in standardized QA labs
- Worked on Varian Linacs and GE CT scanners
- Used Eclipse and Aria software

Shadowing Experience, *IU Health Ball Memorial University Hospital, 2013-14*
Dr. Alvin Foster, Senior Medical Physicist, IU Health Ball Memorial Hospital

- Observed a cervical and prostate brachytherapy procedure
- Controlled Varian Linacs and used Eclipse software
- Observed a medical physicist's day-to-day schedule

RESEARCH EXPERIENCE

Purdue University, *Medical Physics, 2016-Present*
Advisor: Dr. Carlos Perez-Torres
Thesis: *Quantitative analysis of radiation-induced pulmonary fibrosis in mice using diagnostic imaging*

- Conducted research with Bruker Biospec 7T pre-clinical MRI, PerkinElmer Quantum GX µCT, and Precision XRAD-320 cabinet irradiator
- Segmented data using MatLab and ITK-SNAP software
- Statistically analyzed data using GraphPad's Prism software

IU Health-Ball Memorial Hospital, *Department of Radiation Oncology, 2013-14*
Advisor: Dr. Alvin Foster
Thesis: *Cardiovascular implantable electronic device dose estimates for radiotherapy patient management*

- Learned how therapists upload and perform treatment plans on Varian's system
- Determined dosimetry using TLDs attached to anatomical phantom

---

TEACHING EXPERIENCE

Teacher, *Faith Christian School, Lafayette, IN, 2019-20*
- Teaching AP Physics C and AP Physics 1 courses to high school students

Grader, *Indiana and Purdue University, 2014-19*
- Graded for classes in General Physics, Physics of Sound, Quantum Mechanics, Classical Mechanics, Radiation Biology, and Radiation Sciences

Teaching Assistant, *Taylor University, Ball State University, and Purdue University, 2008-14*
- Led discussions and assisted students in multiple lab sections every week
- Created quizzes, graded assignments, and planned pre-lab discussions

Student Teaching, *New Haven High School, New Haven, IN, 2011*
- Full responsibility for three different classes: Algebra I, Integrated Chemistry and Physics, and Physics I
- Worked with a diverse congregation of students in an inner-city high school
- Assisted instructor with a college-credited physics lab for Indiana Purdue Fort Wayne (IPFW)

LEADERSHIP EXPERIENCE

Co-President, *Medical Physics Student Organization, Purdue University, 2019-Present*
- Communicating to student members pertinent information and about events
- Coordinating speakers, discussions, and social events

College Ministry Sponsor, *Purdue Bible Fellowship, Faith Church, 2018-Present*
- Leading weekly Bible studies for college students
- Chaperoning the PBF spring break trip
- Mentoring young men in need of guidance

Tutor, *Independent Service, 2008-18*
- Worked one-on-one with students needing help in physics and math
- Led bi-weekly math and physics study tables

President, *Medical and Biological Physics Student Organization (MaBPSO), Indiana University, 2015-16*
- Led and organized monthly seminars
- Coordinated speakers, discussions, and social events

CONFERENCE PRSENTATIONS

McIlrath, Daniel R. (2019) *Thoracic Radiation Injury Murine Model for Pulmonary Fibrosis.* Presented at the AAPM Ohio River Valley Fall Symposium. Indianapolis, IN.

McIlrath, Daniel R. (2019) *Thoracic Radiation Injury Murine Model for Pulmonary Fibrosis.* Presented at the AAPM Annual Meeting. San Antonio, TX.

McIlrath, Daniel R. (2019) *Murine Radiation-Induced Stomach Pathology for Whole Thoracic Irradiation.* Presented at the AAPM Annual Meeting. San Antonio, TX.

McIlrath, Daniel R. (2018) *Whole Thoracic Radiation Injury Murine MRI Model for Pulmonary Fibrosis*. Presented at the AAPM Annual Meeting. Nashville, TN.

McIlrath, Daniel R. (2017) *Correlation between MRI signal and SPION dose concentration within murine liver.* Presented at the AAPM Ohio River Valley Fall Symposium. Indianapolis, IN.

MANUSCRIPTS

Kobos, L., Alqahtani, S., Xia, L., [et al, including McIlrath, D.] (2020). *Journal of Toxicology and Environmental Health, Part A: Current Issues*.

McIlrath, D. & Perez-Torres, C. (2020). Murine Radiation-Induced Stomach Pathology from Whole Thoracic Irradiation. *International Journal of Radiation Biology*. (*submitted*)

McIlrath, D. & Perez-Torres, C. (2020). Quantification of Murine Radiation-Induced Pulmonary Fibrosis (RIPF) from Whole Thoracic Irradiation. (*planned*)

McIlrath, D. & Perez-Torres, C. (2020). Comparison of CT and MR Imaged Murine Radiation-Induced Pulmonary Fibrosis (RIPF) from Whole Thoracic Irradiation. (*planned*)